



# Structure, morphology and photoluminescence emissions of ZnMoO<sub>4</sub>: RE<sup>3+</sup>=Tb<sup>3+</sup> - Tm<sup>3+</sup> - X Eu<sup>3+</sup> (x = 1, 1.5, 2, 2.5 and 3 mol%) particles obtained by the sonochemical method



L.X. Lovisa<sup>a,\*</sup>, M.C. Oliveira<sup>b</sup>, J. Andrés<sup>b</sup>, L. Gracia<sup>c</sup>, M.S. Li<sup>d</sup>, E. Longo<sup>e</sup>, R.L. Tranquilin<sup>a</sup>, C.A. Paskocimas<sup>a</sup>, M.R.D. Bomio<sup>a</sup>, F.V. Motta<sup>a</sup>

<sup>a</sup> LSQM—Laboratório de Síntese Química de Materiais, DEMAT, UFRN, Natal, Campus, Lagoa Nova, Natal, RN CEP 59078-900, Brazil

<sup>b</sup> Departament de Química Física i Analítica, Universitat Jaume I, Campus del Riu Sec, Castelló E, 12071, Spain

<sup>c</sup> Department of Química-Física, Universitat de València, 46100, Burjassot, Spain

<sup>d</sup> IFSC, USP, Av. Trabalhador São Carlense, 400, CEP 13566-590, São Carlos, SP, Brazil

<sup>e</sup> LIEC, IQ, UNESP, Rua Francisco Degni s/n, CEP 14801-907, Araraquara, SP, Brazil

## ARTICLE INFO

### Article history:

Received 18 January 2018

Received in revised form

19 March 2018

Accepted 29 March 2018

Available online 30 March 2018

### Keywords:

ZnMoO<sub>4</sub>: Tb<sup>3+</sup>

Tm<sup>3+</sup>

Eu<sup>3+</sup>

Sonochemical method

Photoluminescence

## ABSTRACT

ZnMoO<sub>4</sub> and ZnMoO<sub>4</sub>: RE<sup>3+</sup> = 1% Tb<sup>3+</sup>, 1% Tm<sup>3+</sup>, x Eu<sup>3+</sup> (x = 1, 1.5, 2, 2.5 and 3 mol%) particles were prepared by a sonochemical method. The influence of the dopant content on photoluminescent behavior was investigated. The X-ray diffraction results confirmed the formation of the α-ZnMoO<sub>4</sub> phase with a triclinic crystalline structure. The influence of the chemical compositions on photoluminescence emissions has been studied and the results clearly show the specific emissions of Tb<sup>3+</sup> and Eu<sup>3+</sup>, simultaneously, with a strong contribution of the matrix. Band gap values are in the range of 3.55–4.25 eV. From the values calculated for the CIE coordinates, it was observed that this material develops an emission tendency in the orange-red region. It has been demonstrated for the first time that the sample ZnMoO<sub>4</sub>: 1% Tb<sup>3+</sup>, 1% Tm<sup>3+</sup>, 2% molEu<sup>3+</sup>, presented higher photoluminescence intensity. At higher concentrations of RE<sup>3+</sup>, the quenching effect was observed. The morphology of samples are interpreted based on a comparative analysis of the calculated and experimental field emission scanning electron microscopy (FE-SEM) images. First-principle calculations at a density functional theory level were performed to obtain the values of surface energies and relative stability of the (120), (001), (011), (201), and (100) surfaces by employing the Wulff construction. A complete map of the available morphologies of ZnMoO<sub>4</sub> and ZnMoO<sub>4</sub>:12.5%molEu<sup>3+</sup> is obtained and a possible explanation for the transformation processes is provided in which the experimental and theoretical morphologies can match. The present study offers a fundamental knowledge that is expected to enable the fabrication of ZnMoO<sub>4</sub>-based phosphor materials with a controllable emission peak shift and intensity.

© 2018 Elsevier B.V. All rights reserved.

## 1. Introduction

Over the last decades, the interest for molybdates has been increasing due to their potential applications in the most diverse areas, such as biology, photoluminescence, photocatalysis, and lithium ion batteries [1–4]. Rare earth cations, RE<sup>3+</sup>, doped molybdates present high chemical stability, which allows them to be applied in versatile applications, such as plasma display panels, field emission display, lighting industries and white light emitting

diodes [5–9]. Therefore, these materials are considered a new generation of light sources, which have been replacing fluorescent lamps efficiently, due to low energy consumption and fast response.

The doping processes of RE<sup>3+</sup>, the main members of lanthanide's group, at the lattice of the molybdates are responsible for the appearance of optical properties due to 4f valence shell electrons, while photoluminescence emissions are associated to f-f or 4f-5d transitions [10,11], and the emission wavelength also depends on the splitting of energy level. For example, Eu<sup>3+</sup> cations are activated phosphors that provoke a strong red emitter signal due to <sup>5</sup>D<sub>0</sub>→<sup>7</sup>F<sub>2</sub> electric dipole transition [12], while Tb<sup>3+</sup> cations are activated

\* Corresponding author.

E-mail address: [lauraengmat@hotmail.com](mailto:lauraengmat@hotmail.com) (L.X. Lovisa).

phosphors which reads a strong green emission due to the transitions of  $^5D_3$ - $^7F_1$  in the blue and  $^5D_4$ - $^7F_1$  in the green region ( $J = 6, 5, 4, 3, 2$ ) and the transition intensities depend on their critical doping concentrations [13].

On the other hand, it is well known that the co-doping process of  $RE^{3+}$  is an adequate procedure to enhance intensity since in this process the energy transfer occurs from one  $RE^{3+}$  cation which acts as a sensitizer to another  $RE^{3+}$  cation acting as activator. Along this process, the energy transfer between  $RE^{3+}$  cations is possible due to a plethora of effects such as resonant energy transfer, energy transfer by non-radiative transition and quantum cutting [14]. Many combinations of sensitizer and activator of  $RE^{3+}$  were developed as  $Er^{3+}$ - $Yb^{3+}$ ,  $Eu^{3+}$ - $Gd^{3+}$ ,  $Eu^{3+}$ - $Sm^{3+}$  and  $Eu^{3+}$ - $Tb^{3+}$  [15–21].

For the zinc molybdate,  $ZnMoO_4$ , as a representative member of molybdate family, recent experimental and theoretical studies have evaluated in detail their phosphorescent behavior at low temperatures and a crystal phosphor model was proposed to explain the corresponding mechanism [22–24]. In addition, the influence of the growth conditions of the  $ZnMoO_4$  crystals and the characteristics of the decay are analyzed to find an increase of the luminescence emissions [25].  $ZnMoO_4$  is an inorganic semiconductor that present two types of crystal structures: alpha ( $\alpha$ ) and beta ( $\beta$ ) and has been successfully synthesized by different methods, including the sonochemistry, precipitation and hydrothermal processes [26–29]. The type of phase obtained depends on the conditions of synthesis, time, and temperature processing [30]. The crystals  $\alpha$ - $ZnMoO_4$  have a triclinic structure, with space group  $P1$  and group symmetry  $C_1$  [31], in which the Zn cations are coordinated by six oxygen anions that form the distorted octahedral [ $ZnO_6$ ], while Mo cations are bound to four oxygen anions in a tetrahedral configuration [ $MoO_4$ ] [32]. The crystals  $\beta$ - $ZnMoO_4$  have a monoclinic structure of the wolframite type, with space group  $P2_1/c$  and group symmetry  $C_{2h}^4$ . In the monoclinic structure, the Zn and Mo cations are coordinated by six oxygen atoms that form the distorted octahedral [ $ZnO_6$ ] and [ $MoO_6$ ], respectively [33].

Mikhailik et al. [34] proposed that the photoluminescent properties of  $ZnMoO_4$  are related to self-localized excitons and to electron transitions within the anionic molecular complex [ $MoO_4$ ] $^{2-}$ . The emission bands can be associated to radioactive recombination processes of the electron-hole pairs located in the anionic molecular complex [ $MoO_4$ ] $^{2-}$  and this moiety is considered the main constituent element, which defines the optical properties in the visible ultraviolet energy region [35]. Cavalcante et al. [36] attributed that the differences in photoluminescence emission intensities of  $ZnMoO_4$  microcrystals are due to the presence of changes in the particle morphology, crystal size and surface defects.  $RE^{3+}$  doped  $ZnMoO_4$ ,  $ZnMoO_4:RE^{3+}$ , have been widely investigated for possible application in optical devices. According to Ju et al. [37], in their work with  $ZnMoO_4$ : Tb from the co-precipitation method, concluded that the light flux in green is more significant than in red and blue among materials co-doped due to the intense emission of the  $^5D_4 \rightarrow ^7F_5$  ( $Tb^{3+}$ ) at 550 nm and that this type of material exhibits excellent thermal and chemical stability [38–40]. Chengaiah et al. [41] evaluated the effect of  $Dy^{3+}$  dopant concentration on the  $ZnMoO_4$  matrix and observed a mixture of emissions in the yellow and blue regions. Through the determination of the chromaticity coordinates, it was possible to produce a material with emission in white. Ran et al. [42] have already described that the energy transfer efficiency between the  $Bi^{3+}$  sensitizer and the  $Eu^{3+}$  activator in the  $ZnMoO_4$  matrix is associated with the concentration of the dopants and the distance between them, highlighting their performance as photoluminescent material in the use of LEDs white.

In this work, a series of the  $ZnMoO_4$  and  $ZnMoO_4$ : 1%  $Tb^{3+}$ , 1%  $Tm^{3+}$ , x  $Eu^{3+}$  (x = 1, 1.5, 2, 2.5 and 3 mol%) particles were prepared by the sonochemical for the preparation of the  $ZnMoO_4$  and  $ZnMoO_4$ : 1%  $Tb^{3+}$ , 1%  $Tm^{3+}$ , x  $Eu^{3+}$  (x = 1, 1.5, 2, 2.5 and 3 mol%). The synthesized samples were characterized by X-ray diffraction and Rietveld refinements, field emission scanning electron microscopy (FE-SEM) and photoluminescence emissions. They present photoluminescence (PL) emissions and a tunable band gap in the visible light region. The geometries, electronic structures and properties of both  $ZnMoO_4$  and  $ZnMoO_4$ : 12.5%  $Eu^{3+}$  systems have been characterized and discussed in relation to their crystal structural characteristics by using the density functional theory (DFT)-based calculations. Next, a joint experimental and theoretical strategy, developed by us, was employed to obtain a complete map of the morphologies available for both systems. Based on these results, and by changing the values of the energy surfaces of (120), (011), (001), (201), (220), (100), (111) and (112) surfaces, we are able to rationalize the different path followed for these system by which the experimental FE-SEM images and theoretical morphologies can match.

The remainder of this paper is organized as follows: Section 2 describes the experimental procedure and computational details, Section 3 exhibits the computational details; Sections 4 and 5 present the results and conclusions, respectively.

## 2. Experimental procedure and computational details

### 2.1. Materials

Acid Molybdic ( $H_2MoO_4$ ), (Alfa Aesar), zinc nitrate ( $Zn(NO_3)_2 \cdot 6H_2O$ ) (Synth), europium oxide ( $Eu_2O_3$ ) (Alfa Aesar), terbium oxide ( $Tb_4O_7$ ) (Aldrich), thulium oxide ( $Tm_2O_3$ ), nitric acid (Synth), ammonium hydroxide ( $NH_4OH$ ) (Synth) and distilled water were used as received to prepare the  $ZnMoO_4$  and  $ZnMoO_4:RE^{3+}$  particles.

### 2.2. Preparation

Initially, the oxides ( $Eu_2O_3$ ,  $Tb_4O_7$  and  $Tm_2O_3$ ) were dissolved separately in 10 ml of nitric acid to obtain their respective nitrates. Since in the form of oxides, these elements are insoluble in the reaction medium. For the synthesis of the  $ZnMoO_4$  and  $ZnMoO_4:RE^{3+}$  particles, two precursor solutions were prepared: one of molybdenum (solution A) and the other of zinc (solution B). For the two solutions, the starting reagent was dissolved in 40 ml of distilled water. Solution A was exposed to high intensity ultrasound irradiation at 65% amplitude in continuous mode. Then solution B was added to solution A during the ultrasound by dripping in the time interval of every 10 min. After the complete dissolution, the dopants ( $RE^{3+}:Tb^{3+}$ ,  $Tm^{3+}$  and  $Eu^{3+}$ ) in nitrate form were added to the system. Finally,  $NH_4OH$  was added to the solution to stabilize the pH at 8. The solution was centrifuged three times in distilled water and then kept in the oven at a temperature of 80 °C for 24 h for drying. The particles were calcined at 650 °C for 4 h at a heating rate of 10 °C/min.

### 2.3. Characterization

The  $ZnMoO_4$  and  $ZnMoO_4:RE^{3+}$  particles were structurally characterized by XRD using a Shimadzu XRD 7000 instrument with Cu-K $\alpha$  radiation ( $\lambda = 1.5406 \text{ \AA}$ ) in the  $2\theta$  range from 10 to 50° at a scanning rate of  $0.02^\circ \text{ s}^{-1}$ . The morphologies were investigated using field-emission scanning electron microscopy (FEG-SEM; Carl Zeiss, Supra 35- VP Model, Germany) operated at 6 kV. The chemical analyzes were performed on the equipment of Energy

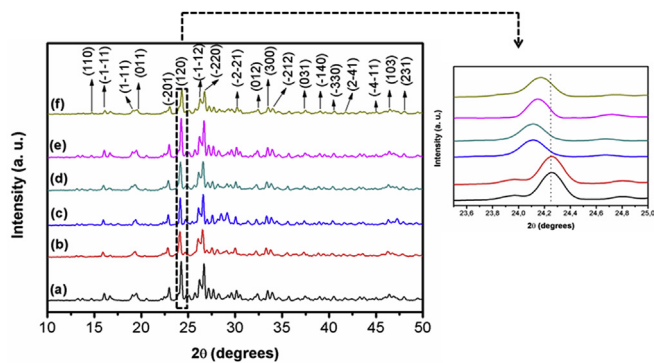


**Fig. 1.** X-ray diffraction of the  $\text{ZnMoO}_4$  materials synthesized by the sonochemical method: (a)  $\text{ZnMoO}_4$ , and  $\text{ZnMoO}_4$ : 1%  $\text{Tb}^{3+}$ , 1%  $\text{Tm}^{3+}$ ,  $x \text{Eu}^{3+}$  % mol: (b)  $x = 1\%$ , (c)  $x = 1.5\%$ , (d)  $x = 2\%$ , (e)  $x = 2.5\%$  and (f)  $x = 3\%$  mol.

Dispersive X-ray Fluorescence Spectrometer EDX-720- Shimadzu. The UV–vis diffuse reflectance spectrum was measured at room temperature using a UV–vis spectrometer. The photoluminescence (PL) spectra were acquired with an Ash Monospec 27 monochromator (Thermal Jarrel, U.S.A.) and a R4446 photomultiplier (Hamamatsu Photonics, U.S.A.). The 350 nm beam of a krypton ion laser (Coherent Innova 90 K) was used as the excitation source while its maximum output power was kept at 200 mW. All measurements were performed at room temperature. The time decay measurements were performed on the equipment Fluorolog3 Horiba Jobin Yvon spectrofluorometer equipped with Hamamatsu R928P photomultiplier, SPEX 1934 D phosphorimeter, and a pulsed 150 W Xe–Hg lamp.

#### 2.4. Computational details

Bulk and surfaces of  $\text{ZnMoO}_4$  and  $\text{ZnMoO}_4$ :12.5% mol  $\text{Eu}^{3+}$  were calculated by means of the hybrid functional B3LYP within the periodic density functional theory (DFT) framework [43,44], using the CRYSTAL14 software package [45]. Eu center was represented by a small-core effective-core pseudopotential (ECP) [46], while Mo center was described by a Hay–Wadt type (basis [HAYWSC]-31G) [47]. Oxygen [48] and zinc [49] centers were both represented by standards at 6-31G\* basis sets.

In the bulk and surface calculations, the exchange–correlation contribution is the result of a numerical integration of the electron density and its gradient, performed over a grid of points. Default values of the tolerances that control the Coulomb exchange series were adopted (ITOL1 = ITOL2 = ITOL3 = ITOL4 = 8, ITOL5 = 14). The Hamiltonian matrix was diagonalized [50], using 36 reciprocal lattice points ( $k$ -points), corresponding to a shrinking

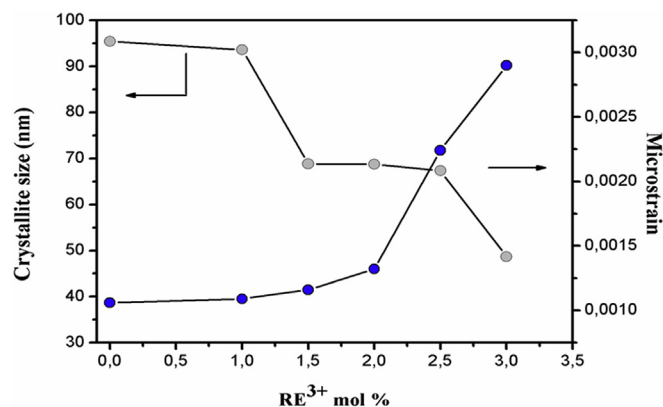


**Fig. 2.** Relationship between crystallite size and microdeformation according to  $\text{RE}^{3+}$  concentration.

factor of  $IS = 4$  method for bulk, while 10  $k$ -points grids were used for surfaces. In this work, a triclinic supercell of 144 and 143 atoms which corresponds to  $1 \times 2 \times 2$  conventional cell, was used to simulate the  $\text{ZnMoO}_4$  and  $\text{ZnMoO}_4$ :12.5%  $\text{Eu}^{3+}$ , respectively. It is important to note that for the calculation of the doped materials,  $\text{ZnMoO}_4$ : $\text{RE}^{3+}$ , we have a technical problem, i.e. because the % of doping is very small, in the range of 1–3 mol%, it is necessary to use very large unit cells. This fact makes calculations computationally very costly, and it was possible to reach a minimum of doping of 12.5%  $\text{Eu}^{3+}$ .

Slab models for (120), (011), (001), (201), (220), (100), (111) and (112) surfaces were considered to obtain the surface energy,  $E_{\text{surf}}$ , values and the morphologies of the  $\text{ZnMoO}_4$  and  $\text{ZnMoO}_4$ :12.5%  $\text{Eu}^{3+}$  systems. Surface calculations were determined from the equilibrium shape by a classic Wulff construction [51] that minimizes the total surface free energy at a fixed volume, providing a simple correlation between the  $E_{\text{surf}}$  of the ( $hkl$ ) plane and the distance,  $r(hkl)$ , in the normal direction from the center of the crystallite. The Wulff construction has been successfully used in materials science to obtain the morphology of materials, including  $\text{PbMoO}_4$ ,  $\alpha\text{-Ag}_2\text{MoO}_4$  as well as  $\text{BaMoO}_4$  materials [52–54].

$E_{\text{surf}}$  is defined as the total energy per repeating slab cell ( $E_{\text{slab}}$ ) minus the total energy of the perfect crystal per molecular unit ( $E_{\text{bulk/atom}}$ ) multiplied by the number of molecular units of the surface ( $N_s$ ) and divided by the surface area ( $A$ ) per repeating cell of the two sides of the slab, as shown in equation (1).

$$E_{\text{suf}} = \frac{1}{2A} (E_{\text{slab}} - N_s \cdot E_{\text{bulk/atom}}) \quad (1)$$

**Table 1**

Crystallographic data of  $\text{ZnMoO}_4$  and  $\text{ZnMoO}_4$ : $\text{RE}^{3+}$  samples.

Samples	$\text{ZnMoO}_4$	$\text{ZnMoO}_4$ (Theoretical)	$\text{ZnMoO}_4$ : 1% Tb 1% Tm 1% mol $\text{Eu}^{3+}$	$\text{ZnMoO}_4$ : 1% Tb 1% Tm 1.5% mol $\text{Eu}^{3+}$	$\text{ZnMoO}_4$ : 1% Tb 1% Tm 2% mol $\text{Eu}^{3+}$	$\text{ZnMoO}_4$ : 1% Tb 1% Tm 2.5% mol $\text{Eu}^{3+}$	$\text{ZnMoO}_4$ : 1% Tb 1% Tm 3% mol $\text{Eu}^{3+}$
$a$ (Å)	9.6822	9.7476	9.6835	9.69991	9.69056	9.70418	9.70166
$b$ (Å)	6.9487	6.9847	6.9518	6.95539	6.96208	6.96021	6.96096
$c$ (Å)	8.3687	8.3984	8.3551	8.3668	8.37362	8.37270	8.37684
$V$ (Å) <sup>3</sup>	563.0352	526.5936	562.127	564.4800	564.9384	565.5183	565.7120
$\alpha$	101.7090	101.3339	101.720	101.6817	101.7214	101.7112	101.6878
$\beta$	96.7422	96.8497	96.847	96.8367	96.7110	96.82299	96.81503
$\theta$	106.86	106.9862	106.851	106.8180	106.8245	106.8004	106.8083
$D$ (nm)	95.448	–	93.570	93.570	68.839	68.736	67.342
$\mathcal{E}$ ( $10^{-3}$ )	1.06	–	1.09	1.16	1.32	2.24	2.9
$R_{\text{wp}}$	6.80	–	8.05	6.93	10.03	8.37	8.54
$R_b$	3.80	–	11.27	12.21	7.49	13.17	6.83
$\chi^2$	0.56	–	1.40	1.28	0.72	1.50	0.80

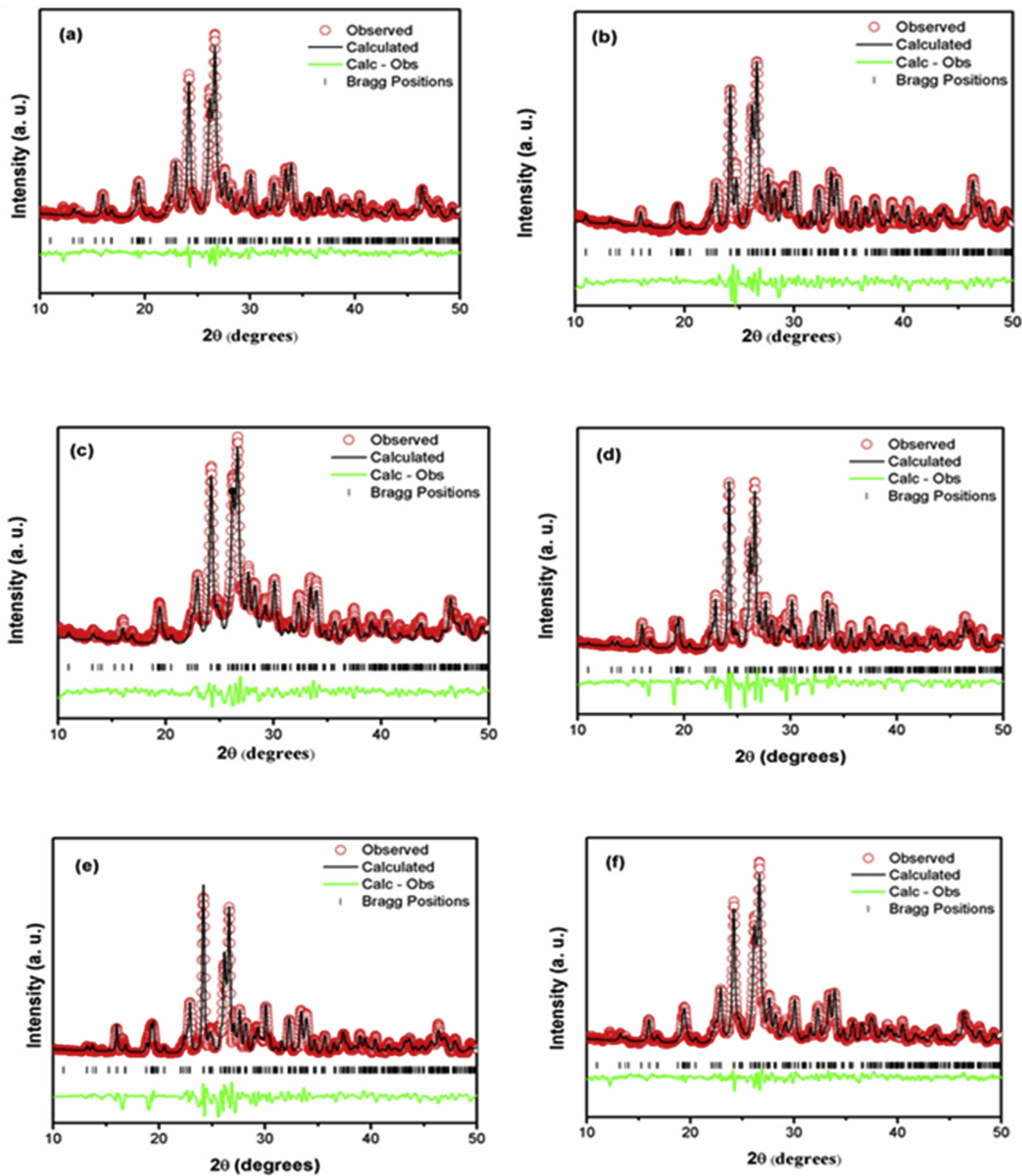


Fig. 3. Structural refinement of the samples (a)  $\text{ZnMoO}_4$ , and  $\text{ZnMoO}_4$ : 1%  $\text{Tb}^{3+}$ , 1%  $\text{Tm}^{3+}$ ,  $x$   $\text{Eu}^{3+}$  % mol: (b) 1%, (c) 1.5%, (d) 2%, (e) 2.5% and (f) 3% mol.

### 3. Results

The XRD pattern presented in Fig. 1 show the diffraction peak characteristics of  $\text{ZnMoO}_4$ . They can be indexed in a triclinic structure of the  $\alpha$  type with space group  $P1$  in  $C_1$  symmetry (JCPDS-35–0765). The XRD patterns of the samples showed that the  $\text{ZnMoO}_4$ :RE are structurally related to the triclinic crystalline phase.

There was no secondary phase formation, indicating that doping occurred successfully.

A decrease in the intensity of the peak (120) at  $24.30^\circ$  is observed in Fig. 1 accompanied by an increase of the amount of dopants in the  $\text{ZnMoO}_4$  matrix. The structural and electronic distortion in the  $[\text{ZnO}_6]$  clusters caused by the substitution of  $\text{RE}^{3+} \rightarrow \text{Zn}^{2+}$  in the structure of  $\text{ZnMoO}_4$  is evidenced by the



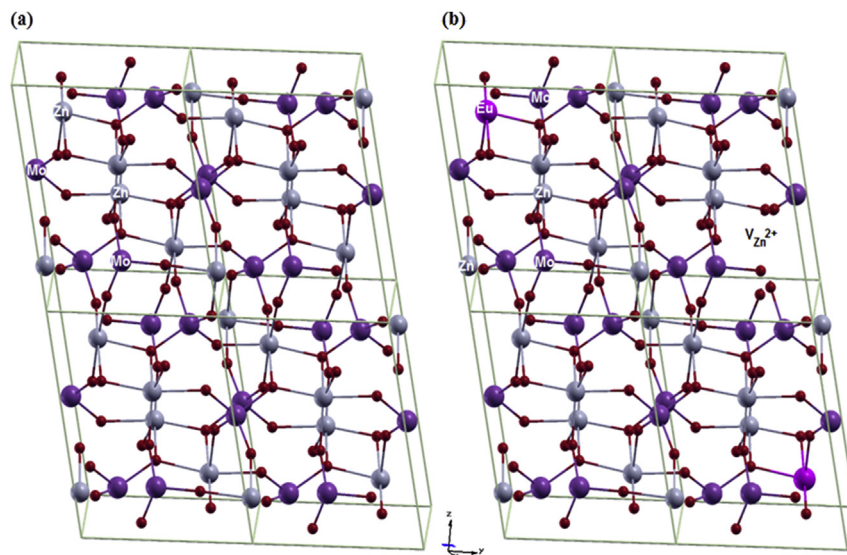


Fig. 4. Theoretical representation of the triclinic  $1 \times 2 \times 2$  supercell corresponding to (a)  $\text{ZnMoO}_4$  and (b)  $\text{ZnMoO}_4:12.5\% \text{ molEu}^{3+}$  crystals.

displacement of the peaks to a region of smaller angle according to Fig. 1. This fact can be associated to the difference in the size between the  $\text{RE}^{3+}$  and  $\text{Zn}^{2+}$  cations. Ju et al. [37] noted that the peaks of the XRD patterns become weak and slightly broad due to the increase of the concentration of  $\text{Tb}^{3+}$  in  $\text{ZnMoO}_4$ .

The values of the mean crystallite size and the micro strain of  $\text{ZnMoO}_4$  and  $\text{ZnMoO}_4:\text{RE}^{3+}$  are shown in Table 1. The mean crystallite size was estimated by the Scherrer equation (2) [55].

$$D_{hkl} = 0.9\lambda / \beta \cos\theta \quad (2)$$

Where  $D_{hkl}$  is the mean crystallite size,  $\lambda$  is the wavelength,  $\theta$  is half the Bragg angle and  $\beta$  is the half height of the selected reflection (FWHM). The reduction in the crystallite size is verified when the dopant concentration is increased as shown in Fig. 2. This behavior is first of all due to the distortion caused in the  $\text{ZnMoO}_4$  lattice by the dopants, which can slow down the growth of the crystals [56]. According to Vidya et al. [57], the dopant provides a lagging force in the grain boundaries. If this generated retarding force is greater than the grain growth force by the formed ion of the lattice (Zn), then the diffusibility is reduced. The micro strain is associated to the synthesis conditions that the materials were formed. For example, the fast precipitation of the  $\text{ZnMoO}_4$  particles due to the strong attraction force between  $\text{Zn}^{2+}$  or  $\text{RE}^{3+}$  and  $(\text{MoO}_4)^{2-}$  ions due to the addition of  $\text{NH}_4\text{OH}$ . The bonds that form later can generate defects and deformation in the crystals.

The Rietveld refinement method was used to explain possible differences in the structural arrangements induced by the processing of  $\text{ZnMoO}_4$  and  $\text{ZnMoO}_4:\text{RE}^{3+}$  particles. This refinement was performed by using the general structure analysis Maud program version 2.0. The results of the Rietveld refinements are shown in Fig. 3. The measured diffraction patterns are well matched to ICSD 1528282. The diffractogram corresponding to the experimental and theoretically calculated data are practically identical, as shown in the Calc-Obs line. The results of the refinement are summarized in Table 1. The high quality of the refinement is revealed by the reliability parameters ( $X^2$ ,  $R_{wp}$  and  $R_p$ ). The Rietveld method uses the profiles of the intensities obtained by the slow scan measurements of the material from the X-ray diffraction technique.

The cell and atomic position parameters used in the calculations

are taken from the results of the Rietveld refinements for both structures (Table 1). An optimization of the cell parameters was performed and the unit cell representation was modeled using a single conventional  $1 \times 2 \times 2$  cell for  $\text{ZnMoO}_4$  and  $\text{ZnMoO}_4:\text{Eu}^{3+}$  materials. The X-Window Crystalline Structures and Densities (XCrySDen) program [58] were used to design the periodic model, as showed in Fig. 4(a and b).

The determination of the value of the gap energy ( $E_{\text{gap}}$ ) for the  $\text{ZnMoO}_4:\text{RE}^{3+}$  particles was performed from the UV–Visible spectroscopy by the diffuse reflectance mode. The obtained reflectance data were converted to absorbance [ $F(R) = \alpha$ ], generating an absorbance versus energy (eV) plot as indicated in Fig. 5. The values of  $E_{\text{gap}}$  were obtained from the linear extrapolation following the Tauc and Wood method [50].

The electronic transitions in the materials happen through the energy bands and are followed by the emission or absorption of photons in the crystal. For a crystal to have direct electronic transitions, it is necessary to observe the conservation of energy and momentum in the crystal. This condition is favored when the maximum of the valence band (VB) and the minimum of the conduction band (CB) are in the same region of symmetry of the solid. According to different authors [35,59,60], the  $\text{ZnMoO}_4$  crystals exhibit an optical absorption spectrum governed by direct electronic transitions. We calculated and plotted the band structure of  $\text{ZnMoO}_4$  and  $\text{ZnMoO}_4:12.5\% \text{ molEu}^{3+}$  along various high-symmetry directions in the first Brillouin zone as shown in Fig. 6(a and b). An analysis of the results displayed in this Figure points out that the doping of  $\text{Eu}^{3+}$  provokes a decrease of the values for the energy levels belonging to CB with respect to pure  $\text{ZnMoO}_4$ ; the energy range is 5.5–6.0 eV and 2–7–3.6 eV for  $\text{ZnMoO}_4$  and  $\text{ZnMoO}_4:12.5\% \text{ molEu}^{3+}$ , respectively; while the distribution of energy levels within both CB and VB are more compact at  $\text{ZnMoO}_4$  with respect to  $\text{ZnMoO}_4:12.5\% \text{ molEu}^{3+}$ .

The experimental values found for  $E_{\text{gap}}$  are in the range of 3.55 and 4.25 eV, while theoretical calculations predict an indirect gap of 5.28 and 2.67 eV for  $\text{ZnMoO}_4$  and  $\text{ZnMoO}_4:\text{Eu}^{3+}(12.5\%)$  systems, respectively. Fig. 6a–b reveals that the indirect transition is produced along the  $k$ -points  $F \rightarrow G$  (010–001) from the top of VB to the bottom of CB, although the band structure for the doped system is very flat. The projected total DOS for  $\text{ZnMoO}_4$  and  $\text{ZnMoO}_4:12.5\% \text{ molEu}^{3+}$  are presented in Fig. 7a and b, respectively. An analysis of

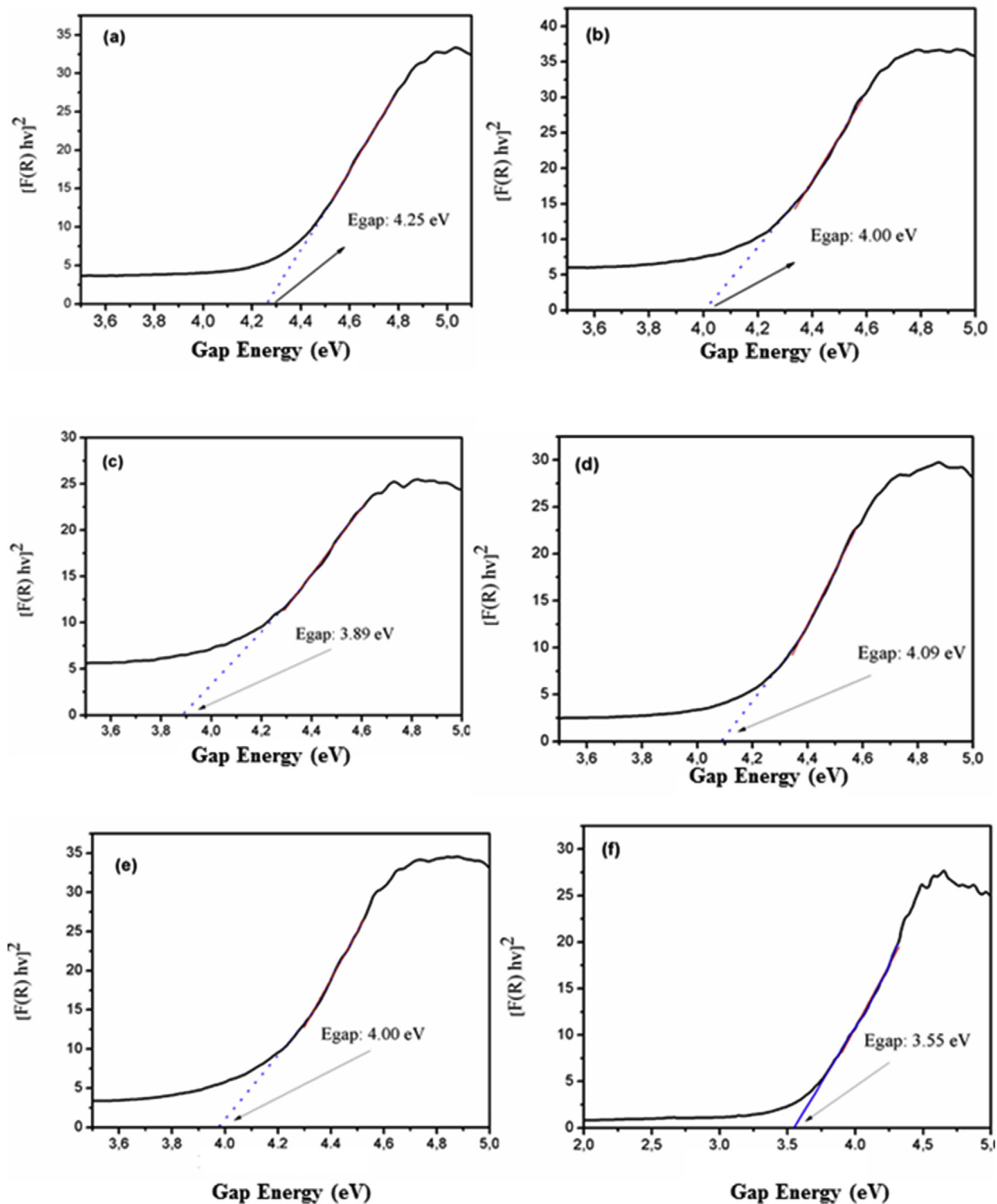


**Fig. 5.** Determination of the gap energy value by using the Tauc and Wood method: (a)  $\text{ZnMoO}_4$  and  $\text{ZnMoO}_4$ : 1%  $\text{Tb}^{3+}$ , 1%  $\text{Tm}^{3+}$ , x  $\text{Eu}^{3+}$  mol; (b) x = 1%, (c) x = 1.5%, (d) x = 2%, (e) x = 2.5% and (f) x = 3% mol.

these figures shows that the VB from 0 to  $-0.67\text{eV}$  ( $\text{ZnMoO}_4$ ) and from 0 to  $-0.89\text{eV}$  ( $\text{ZnMoO}_4$ : 12.5% mol  $\text{Eu}^{3+}$ ) are composed mainly of O orbitals (px, py and pz). CB is mainly formed by the Mo and Eu orbitals with a lower contribution of the Zn orbitals ( $d_{z^2}$ ,  $dx^2-y^2$ , dxy, dxz, dyz), located in the range from 5.28 to 6.07 eV ( $\text{ZnMoO}_4$ )

and from 2.67 to 3.57 eV ( $\text{ZnMoO}_4$ : 12.5% mol  $\text{Eu}^{3+}$ ).

The substitution of the  $\text{RE}^{3+}$  cations by  $\text{Zn}^{2+}$  cations promotes an unbalance in the charges within the crystalline structure of  $\text{ZnMoO}_4$  because the oxidation states of the cations are different. As a way of restoring material neutrality, structural defects occur. The

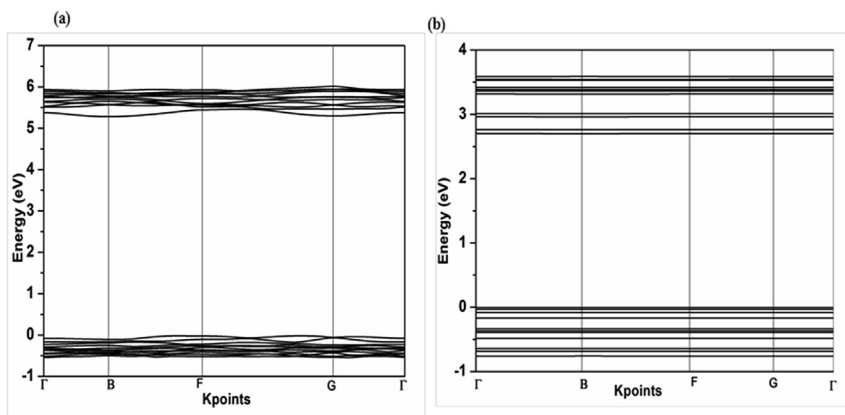


Fig. 6. Band structure of (a) ZnMoO<sub>4</sub> and (b) ZnMoO<sub>4</sub>:12.5 molEu<sup>3+</sup> crystals.

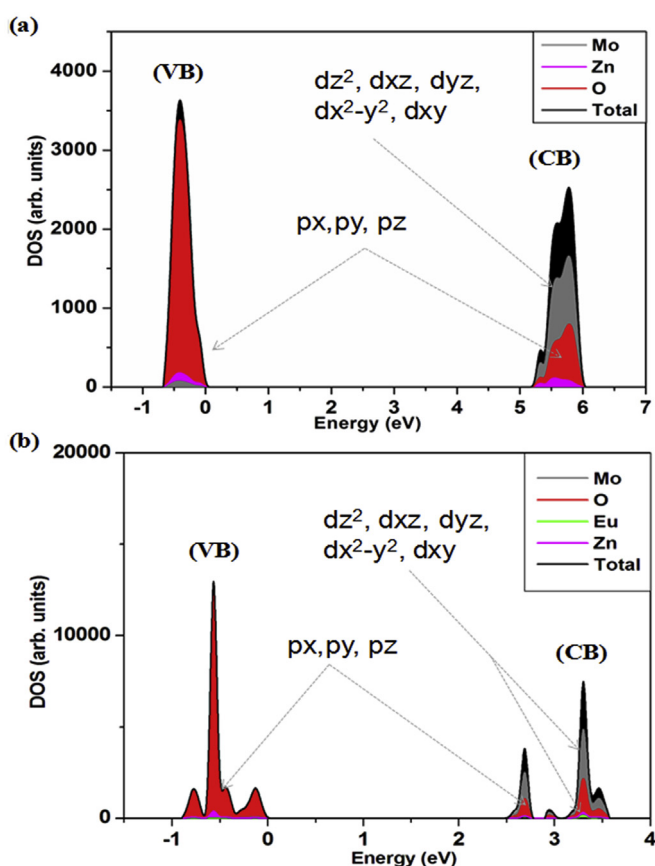


Fig. 7. Projected total DOS of (a) ZnMoO<sub>4</sub> and (b) ZnMoO<sub>4</sub>: 12.5% molEu<sup>3+</sup>.

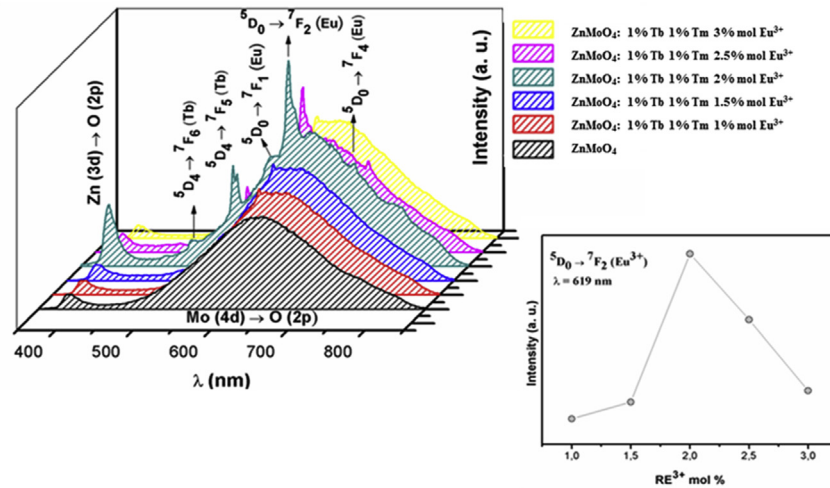
RE<sup>3+</sup> cations when incorporated to the ZnMoO<sub>4</sub> matrix causes an excess of positive charges, then, Zn<sup>2+</sup> vacancies appear [41,61,62]. From an electronic perspective, the presence of these defects promotes the presence of intermediate electronic levels in the forbidden region. This new band gap configuration contributes to electronic transitions occurring at a lower energy level. Fig. S1 (of Supporting Information) represents the decrease in the E<sub>gap</sub> with increasing dopant concentration. It is observed that there is no linearity in the relationship between the two parameters. It is reasonable to consider that other factors may interfere, such as the synthesis method as well as the morphology of the particles.

Fig. 8 presents the photoluminescence emission spectrum of the

ZnMoO<sub>4</sub> and ZnMoO<sub>4</sub>:RE<sup>3+</sup> particles. The samples were excited by a laser of  $\lambda = 350$  nm at room temperature. An analysis of the results displayed in Fig. 8 renders a first band of lower intensity located between 370 and 419 nm, which can be associated to the recombination of the hole–electron pairs within the clusters [ZnO<sub>6</sub>] with predominant emission in violet. A second band of higher intensity is observed located between 475 nm and 850 nm with a peak at 640 nm. Sczancoski et al. [35] consider that the energy states of the molybdate crystals are formed by oxygen states (2p) located above the VB and molybdenum states (4d) located under the CB as shows in Fig. 7. The electronic transitions of type Mo (4d) → O (2p) may present different emissions according to the positioning of the holes in the band structure. This second band was decomposed into four emission bands indicating the contribution of each band of the visible spectrum to the photoluminescence behavior, according to the deconvolutions shown in Fig. 9. The transition corresponding to the first deconvolution band is associated with the shallow holes (near the VB) related to O 2p orbitals with dominance in green. While the orange, red and infrared emissions, corresponding to the second, third and fourth bands, are associated to the deep holes (slightly away from the VB) connected to the O 2p orbital [63].

Wu et al. [64] pointed out that the active vibration modes of the Jahn-Teller T<sub>2</sub> symmetry effect may influence the [MoO<sub>4</sub>]<sup>2-</sup> complex of slightly distorted tetrahedral symmetry, which would result in a structured absorption band for the electronic transitions type <sup>1</sup>A<sub>1</sub> → <sup>1</sup>T<sub>2</sub>. Ding et al. [65] have established that the blue emissions are caused by <sup>1</sup>A<sub>1</sub> → <sup>1</sup>T<sub>2</sub> electronic transitions in groups of intrinsic tetrahedra [MoO<sub>4</sub>]<sup>2-</sup> and green emissions by structural defects of the Frenkel type exist on the surface layer of the crystals.

The origin and the mechanisms responsible for the photoluminescence emissions of molybdates are not yet fully understood. Several hypotheses supported by experimental and theoretical results are reported in the literature to explain this optical property. Campos et al. [66], through theory calculations, propose that the CaMoO<sub>4</sub> particles emission processes may be related to the existence of distorted groups [MoO<sub>3</sub>] and [MoO<sub>4</sub>] in the lattice. These authors have argued that these groups lead to the formation of localized levels of energy in the band gap. Marques et al. [67] associate the dependence of photoluminescent properties with the structural order disorder of molybdate prepared by the polymeric precursor method. Ryu et al. [68] verified that both the degree of crystallization and morphology are two important factors in the photoluminescence emissions of BaMoO<sub>4</sub> particles, while Sczancoski et al. [35] suggest that the nature of these emissions are very dependent on the local atomic organizations in the structure.



**Fig. 8.** Photoluminescence emission spectra of the particles (a)  $\text{ZnMoO}_4$ , and  $\text{ZnMoO}_4$ : 1%  $\text{Tb}^{3+}$ , 1%  $\text{Tm}^{3+}$ ,  $x \text{Eu}^{3+}$  mol: (b)  $x = 1\%$ , (c)  $x = 1.5\%$ , (d)  $x = 2\%$ , (e)  $x = 2.5\%$  and (f)  $x = 3\%$  mol; detail of quenching effect on transition  ${}^5\text{D}_0 \rightarrow {}^7\text{F}_2 (\text{Eu}^{3+})$ .

**Fig. 8** shows the emission bands for specific  $\text{RE}^{3+}$  transitions. For  $\text{Tb}^{3+}$ , they are  ${}^5\text{D}_4 \rightarrow {}^7\text{F}_j$  ( $j = 6, 5$ ) located at 490 and 546 nm, respectively. The typical transitions of  $\text{Eu}^{3+}$   ${}^5\text{D}_0 \rightarrow {}^7\text{F}_j$  ( $j = 1, 2$  and 4) are positioned at 590, 619 and 624, 702 nm, respectively, while the bands located at 619 and 624 can be attributed to the  ${}^5\text{D}_4 \rightarrow {}^7\text{F}_2 (\text{Eu}^{3+})$  transition. Speghini et al. [69a] proposed that the transitions are dependent on the symmetry of the sites in which the  $\text{Eu}^{3+}$  is positioned.

The  ${}^5\text{D}_0 \rightarrow {}^7\text{F}_1$  transition of  $\text{Eu}^{3+}$  is a magnetic dipole transition. Its intensity is not influenced by the symmetry of the site. The  ${}^5\text{D}_0 \rightarrow {}^7\text{F}_2$  transition is known as hypersensitive transition and it is greatly influenced by the local symmetry of the  $\text{Eu}^{3+}$  cation and the nature of the host matrix. As a consequence,  $\text{Eu}^{3+}$  dopants can also be used as sensitive probes of local structural symmetry [70]. The asymmetric ratio ( $R$ ) was calculated considering the ratio between the integrals of the areas under curves  ${}^5\text{D}_0 \rightarrow {}^7\text{F}_2$  and  ${}^5\text{D}_0 \rightarrow {}^7\text{F}_1$ , according to equation (3), to investigate the symmetry environment of the  $\text{Eu}^{3+}$  cation site.

$$R = \frac{I(5\text{D}_0 \rightarrow 7\text{F}_2)}{I(5\text{D}_0 \rightarrow 7\text{F}_1)} \quad (3)$$

The calculated  $R$  was 1.70. It is observed that the peak of emission of electric dipole at 619 nm dominates the peak of emission of magnetic dipole at 590 nm, which is mainly due to the occupation of  $\text{Eu}^{3+}$  cations without symmetry inversion [71].

The introduction of the  $\text{RE}^{3+}$  in the  $\text{ZnMoO}_4$  favors the photoluminescence emissions as it is observed in **Fig. 8**. For concentrations higher than that one of the sample  $\text{ZnMoO}_4$ : 1%  $\text{Tb}$  1%  $\text{Tm}$  2% mol  $\text{Eu}^{3+}$ , a significant drop in intensity can be sensed. This effect is related to a critical concentration which is known as the quenching concentration (see details in **Fig. 8**). In this critical concentration the distance  $\text{RE}^{3+} \cdots \text{RE}^{3+}$  is reduced, which favors the emergence of non-radioactive transitions by a process of cross relaxation [72]. Non-radioactive transitions are expressed in phonon forms, which result in vibrations within the crystal lattice. Wang [73] states that the concentration of the dopant determines the average distance between the two neighboring activator cations as well as the photoluminescence efficiency of  $\text{RE}^{3+}$  in doped systems.

A decrease in the emission intensity shows the occurrence of energy migration between  $\text{RE}^{3+}$  in different sites in the lattice, resulting in concentration quenching. Thus, an optimum concentration for  $\text{RE}^{3+}$  is found to be 4 mol% ( $X_c = 0.04$ ). The concentration

quenching occurs by the non-radiative migration of energy between the  $\text{RE}^{3+}$  cations. The migration of non-radiative energy can take place from two distinct mechanisms: i. e (i) Forster resonance energy transfer (multipole–multipole interaction) and (ii) Dexter mechanism (exchange interaction) [74].

For the Forster resonance energy transfer to be characterized in a system it is necessary that: the donor (**D**) is in the excited state and that the distance between the donor and the activator ion (**A**) is a factor of great influence for the transfer power. The specific conditions must be fulfilled for this mechanism to take place. Note the following points: (I) the emission range of **D** is partially superimposed on the absorption range of **A**, and (II) the distance (**Rc**) between **D** and **A** must be sufficiently short, since the energy transfer efficiency is proportional to  $\frac{1}{Rc^6}$ , to allow the interaction of the multipole–multipole emission bands of material [75,76]. The Forster resonance energy transfer can usually happen at distances of up to 100 Å. Dexter (also known as exchange or coalitional energy transfer) is another dynamic quenching mechanism. Dexter energy transfer is a short-range phenomenon ( $Rc = 10 \text{ \AA}$ ) that decreases with  $e^{-R}$  and depends on spatial overlap of donor and quencher molecular orbitals [74].

The critical energy transfer distance ( $Rc$ ) for  $\text{ZnMoO}_4:\text{RE}^{3+}$  was estimated by equation (4) suggested by Blasse [77] from the parameters of the structure, namely the unit cell volume ( $V$ ), the number of units of the molecular formula per unit cell ( $Z$ ) and the quenching concentration ( $Xc$ ).

$$Rc \approx 2 \left[ \frac{3V}{4Xc\pi Z} \right]^{1/3} \quad (4)$$

For the  $\text{ZnMoO}_4$  system: 1%  $\text{Tb}$  1%  $\text{Tm}$  2% mol  $\text{Eu}^{3+}$ , the following values were considered:  $Z = 6$ ,  $V = 564.9384 \text{ \AA}^3$  and  $Xc = 0.04$ , the calculated  $Rc$  was 16.50 Å. Normally, the exchange interaction is preferably in an energy transfer process when the value of  $Rc$  is between 5 and 10 Å [78]. In case of values higher than 10 Å, there is no indication of exchange interaction in this mechanism. Consequently, other multipolar electrical interactions are responsible for the quenching effect between two more activating ions ( $\text{RE}^{3+}$ ).

To characterize the light emitted by the  $\text{ZnMoO}_4$  and  $\text{ZnMoO}_4:\text{RE}^{3+}$  particles, the chromaticity coordinates ( $X_c, Y_c$ ) were calculated as the basis for the distribution of the photoluminescence emission spectrum as established by the



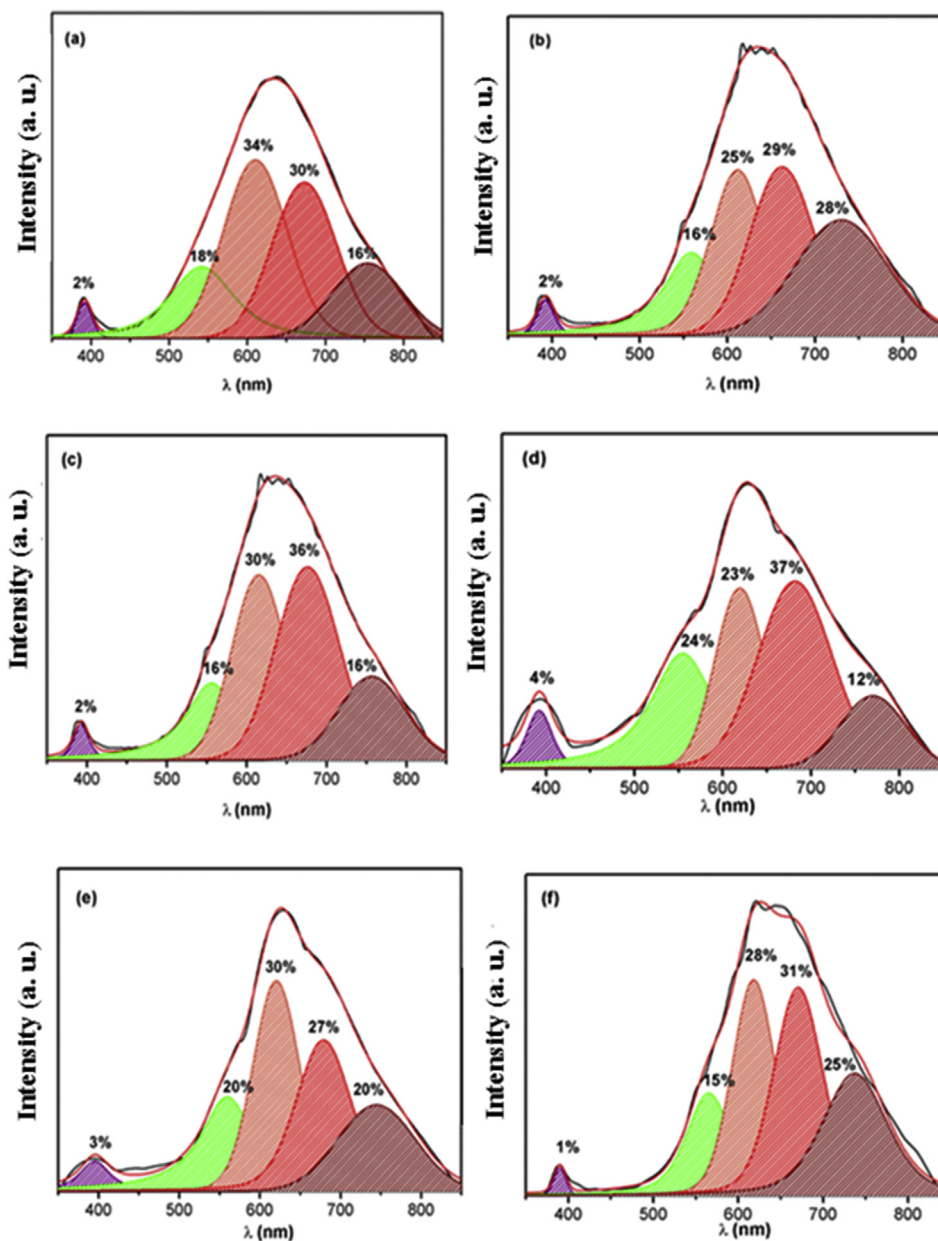


**Fig. 9.** Deconvolutions of the photoluminescence emission spectra of the particles (a)  $\text{ZnMoO}_4$ ;  $\text{ZnMoO}_4$ : 1%  $\text{Tb}^{3+}$ , 1%  $\text{Tm}^{3+}$ ,  $x$   $\text{Eu}^{3++}$  mol: (b)  $x = 1\%$ , (c)  $x = 1.5\%$ , (d)  $x = 2\%$ , (e)  $x = 2.5\%$  and (f)  $x = 3\%$  mol.

international commission on illumination (CIE) [79,80]. As well as, the correlative color temperature (CCT) of each sample was estimated using McCamy's empirical formula [81].

$$\text{CCT} = -449n^3 + 3525n^2 - 6823n + 5520.33 \quad (5)$$

where  $n = \frac{(x-x_e)}{(y-y_e)}$  is the inverse slope line,  $x_e = 0.332$  and  $y_e = 0$ .

The color reproduction index (CRI) is a quantity that measures the ability of a light source to reveal the colors of various objects faithfully compared to an ideal or natural light source. This index ranges from 0 to 100%, the closer to 100% the greater the color accuracy of objects. Fig. 10 represents the chromaticity diagram representing the points of the CIE coordinates (Xc, Yc) of all samples. Table 2 shows the CIE, CCT and CRI coordinates of the  $\text{ZnMoO}_4$  and  $\text{ZnMoO}_4$ : $\text{RE}^{3+}$  particles.

The decay was recorded for  ${}^5\text{D}_0 \rightarrow {}^7\text{F}_2$  transition of  $\text{Eu}^{3+}$  at 614 nm emission. The decay curves of all the  $\text{ZnMoO}_4$ : $\text{RE}^{3+}$  samples exhibited bi-exponential decay as shown in Fig. 11 and have been fitted into exponential equation (6). The average lifetime for the bi-exponential decay was calculated from the following formula (7), the calculated decay parameters are listed in Table 3.

$$I = A_1 \exp\left(-\frac{t}{\tau_1}\right) + A_2 \exp\left(-\frac{t}{\tau_2}\right) \quad (6)$$

Where  $I$  is the emission intensity at any time " $t$ " after switching off the excitation illumination,  $A_1$ ,  $A_2$  are constant.  $\tau_1$ ,  $\tau_2$  are the bi-exponential component of the decay time. The average lifetime for 614 nm emission can be determined by the following formula (6):

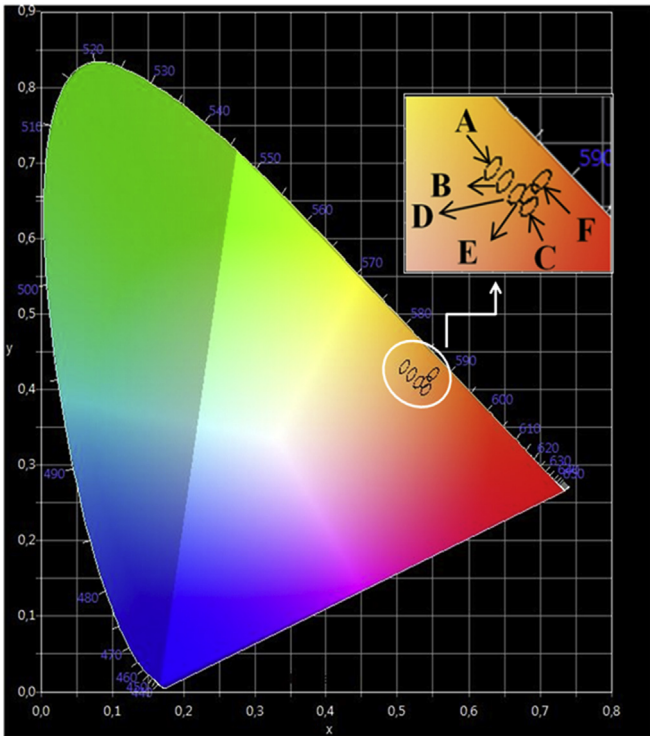


Fig. 10. Chromaticity diagram.

$$\tau = \frac{(A_1 \cdot \tau_1^2) + (A_2 \cdot \tau_2^2)}{A_1 \cdot \tau_1 + A_2 \cdot \tau_2} \quad (7)$$

And the energy transfer efficiency from host to RE<sup>3+</sup> can be calculated according to equation (8) [82]:

$$n = \left(1 - \frac{\tau}{\tau_0}\right) \times 100\% \quad (8)$$

Where  $\tau$  and  $\tau_0$  is the corresponding emission lifetimes of the donor in the presence and absence of the acceptor (RE<sup>3+</sup>) for the same donor concentration, respectively. The energy transfer efficiency from the host to RE<sup>3+</sup> in ZnMoO<sub>4</sub> is 43% for sample of ZnMoO<sub>4</sub>: 1% Tb<sup>3+</sup> 1% Tm<sup>3+</sup> 2% mol Eu<sup>3+</sup>, that exhibited better luminescence.

From the FE-SEM images, it was possible to identify the modifications the morphologies of ZnMoO<sub>4</sub> and ZnMoO<sub>4</sub>:RE<sup>3+</sup>, as well as to estimate the particle size distribution. Chemical analyzes were performed from the x-ray fluorescence spectroscopy of samples ZnMoO<sub>4</sub> and ZnMoO<sub>4</sub>: 1% Tb<sup>3+</sup> 1% Tm<sup>3+</sup> 3% mol Eu<sup>3+</sup>, proving the existence of the elements Zn, Mo, O, Eu, Tm and Tb.

For the sample of pure ZnMoO<sub>4</sub>, it is observed that the particles have plate morphologies, according to the measurements specified in Fig. 12 (I). A similar morphology is found for the sample of

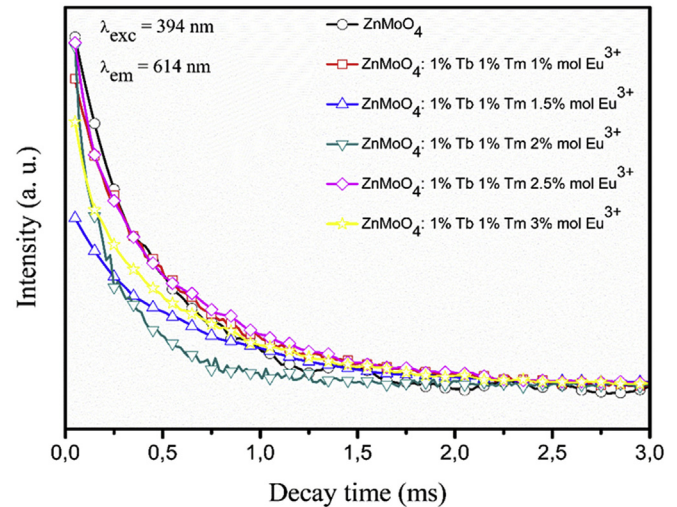


Fig. 11. Decay curves of ZnMoO<sub>4</sub> and ZnMoO<sub>4</sub>: RE<sup>3+</sup>.

ZnMoO<sub>4</sub>: 1% Tb<sup>3+</sup> 1% Tm<sup>3+</sup> 1% mol Eu<sup>3+</sup>. For ZnMoO<sub>4</sub>: 1% Tb<sup>3+</sup> 1% Tm<sup>3+</sup> 1.5% mol Eu<sup>3+</sup>, it was identified octahedral particles with well defined facets. The ZnMoO<sub>4</sub>: 1% Tb<sup>3+</sup> 1% Tm<sup>3+</sup> 2% mol Eu<sup>3+</sup> particles exhibited two different types of morphology and octahedral and cubic shape can be sensed. Through the detail of Fig. 12 (IV), it can be seen the appearance of cubic structures, evidencing the change in the morphology of the particles. The cubic-shaped particles are most relevant for the sample ZnMoO<sub>4</sub>: 1% Tb<sup>3+</sup> 1% Tm<sup>3+</sup> 2.5% Eu<sup>3+</sup>, confirming the trend presented in the previous sample. Moreover, it was possible to identify other forms: hexagonal and octahedral shapes. The sample ZnMoO<sub>4</sub>: 1% Tb<sup>3+</sup> 1% Tm<sup>3+</sup> 3% Eu<sup>3+</sup> presented particles with cubic and hexagonal shapes.

It is well known that the control of the particle growth process is complex and very sensitive to the chemical environment and the internal crystalline structures [83]. The precursor type may be selectively adsorbed on specific exposed surface planes, thereby changing the surface energies and then an inhibition of the appearance of some surface particles along the growth process takes place. Huo [84] stated that the crystallographic planes exposed during the crystal growth process will rapidly decrease during the process as a result of the minimization of the surface energy of the small crystals, which eventually disappear or decrease their participation in the generated morphology. Thus, the surface is generally surrounded by planes with lower surface energies, resulting in slower crystal growth [85].

The equilibrium shape of ZnMoO<sub>4</sub> and ZnMoO<sub>4</sub>: RE<sup>3+</sup> crystals can be calculated using the classic Wulff construction, which minimizes the total surface free energy at a fixed volume, and provides a simple relationship between the  $E_{surf}$  of the (hkl) plane and its distance in the normal direction from the center of the crystallite.

The surface structure and energy values for the (120), (011), (001), (201), (220), (100), (111) and (112) surfaces are described in

Table 2

CIE, CCT and CRI coordinates of ZnMoO<sub>4</sub> and ZnMoO<sub>4</sub>: RE<sup>3+</sup> samples.

Code	Samples	(Xc, Yc)	CCT (K)	CRI	Color
A	ZnMoO <sub>4</sub>	(0.51, 0.43)	2256	87	Orange
B	ZnMoO <sub>4</sub> : 1% Tb 1% Tm 1% mol Eu <sup>3+</sup>	(0.53, 0.41)	1953	84	
C	ZnMoO <sub>4</sub> : 1% Tb 1% Tm 1.5% mol Eu <sup>3+</sup>	(0.54, 0.41)	1876	84	
D	ZnMoO <sub>4</sub> : 1% Tb 1% Tm 2% mol Eu <sup>3+</sup>	(0.52, 0.42)	2099	93	
E	ZnMoO <sub>4</sub> : 1% Tb 1% Tm 2.5% mol Eu <sup>3+</sup>	(0.54, 0.40)	1818	81	
F	ZnMoO <sub>4</sub> : 1% Tb 1% Tm 3% mol Eu <sup>3+</sup>	(0.55, 0.42)	1861	82	

**Table 3**  
Comparison of emission lifetimes of ZnMoO<sub>4</sub> and ZnMoO<sub>4</sub>: RE<sup>3+</sup>.

Samples	$\lambda_{exc}$ (nm)	$\lambda_{em}$ (nm)	$A_1$	$\tau_1$ (ms)	$A_2$	$\tau_2$ (ms)	$\tau$ (ms)
ZnMoO <sub>4</sub>	394	614	79.87	0.15	230.29	0.50	0.47
ZnMoO <sub>4</sub> : 1% Tb 1% Tm 1% mol Eu <sup>3+</sup>	394	614	1054.57	0.70	655.03	0.21	0.62
ZnMoO <sub>4</sub> : 1% Tb 1% Tm 1.5% mol Eu <sup>3+</sup>	394	614	384.89	0.31	522.19	0.89	0.77
ZnMoO <sub>4</sub> : 1% Tb 1% Tm 2% mol Eu <sup>3+</sup>	394	614	1251.93	0.28	722.74	0.03	0.26
ZnMoO <sub>4</sub> : 1% Tb 1% Tm 2.5% mol Eu <sup>3+</sup>	394	614	620.42	0.09	1260.92	0.63	0.59
ZnMoO <sub>4</sub> : 1% Tb 1% Tm 3% mol Eu <sup>3+</sup>	394	614	985.03	0.65	488.45	0.08	0.62

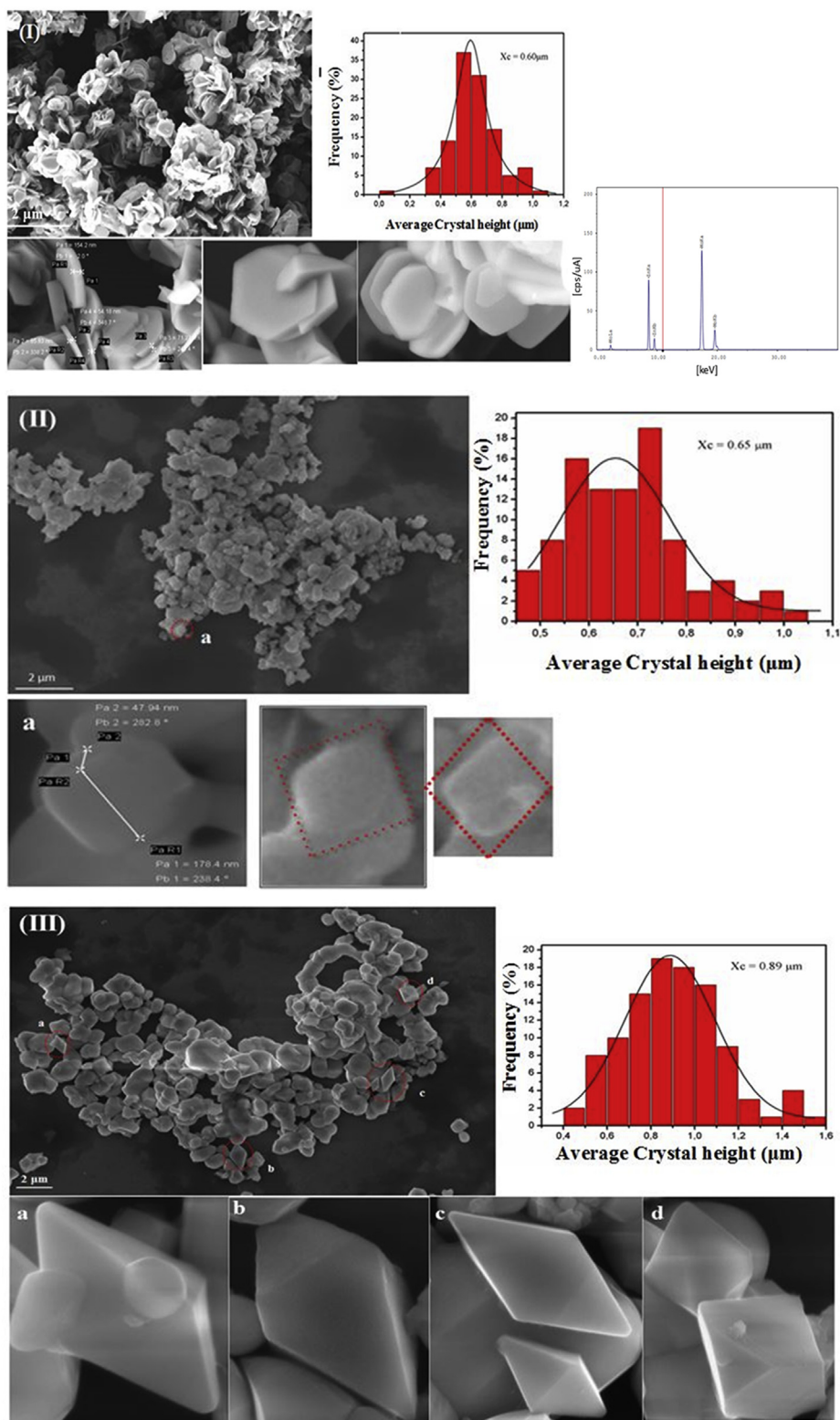


**Fig. 12.** SEM-FEG images for samples ZnMoO<sub>4</sub> (I), and ZnMoO<sub>4</sub>: 1% Tb<sup>3+</sup>, 1% Tm<sup>3+</sup>, x Eu<sup>3+</sup> 3% mol: x = 1% mol (II), x = 1.5% mol (III), x = 2% mol (IV), x = 2.5% mol (V), and x = 3% mol (VI).



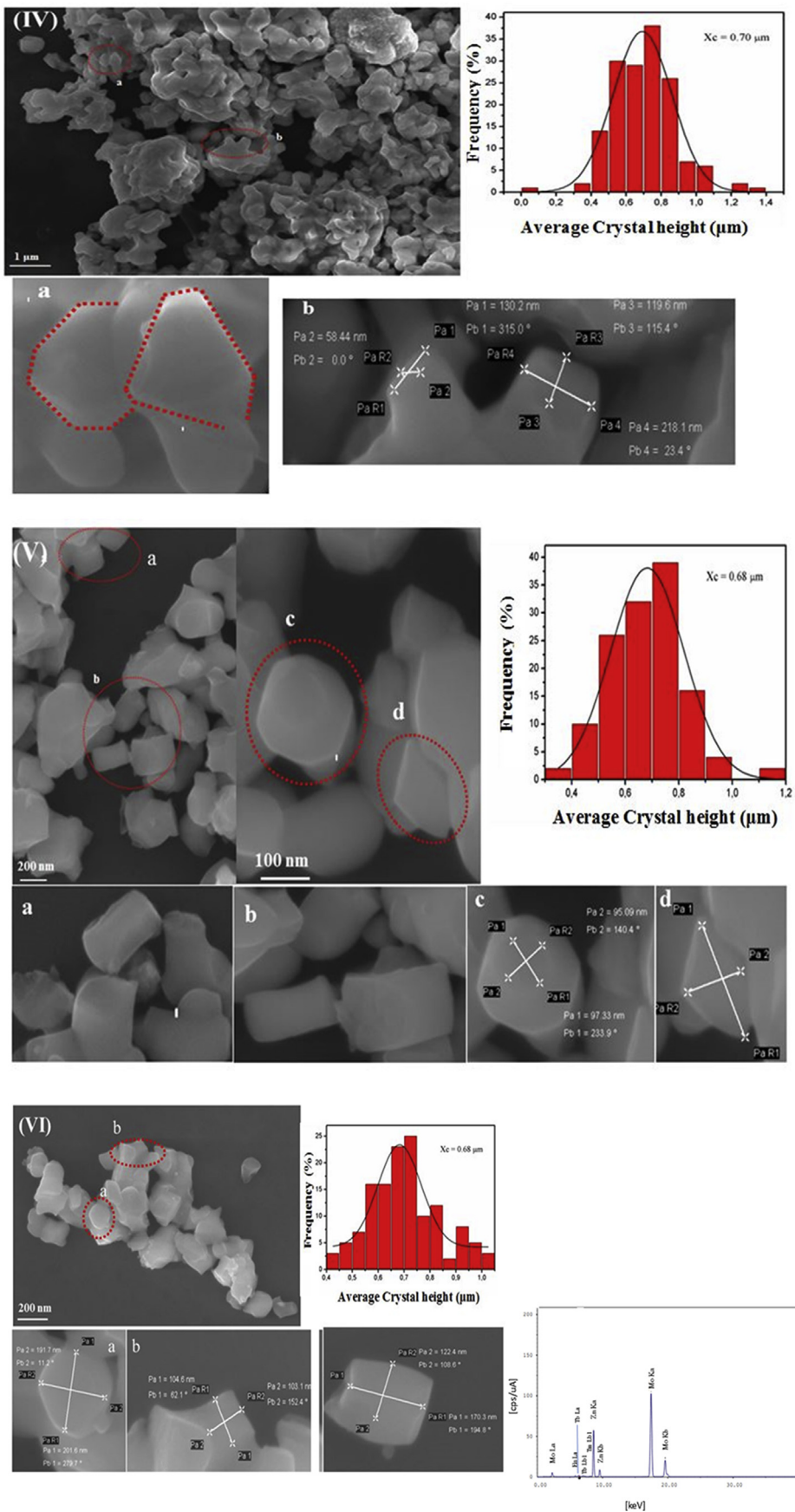
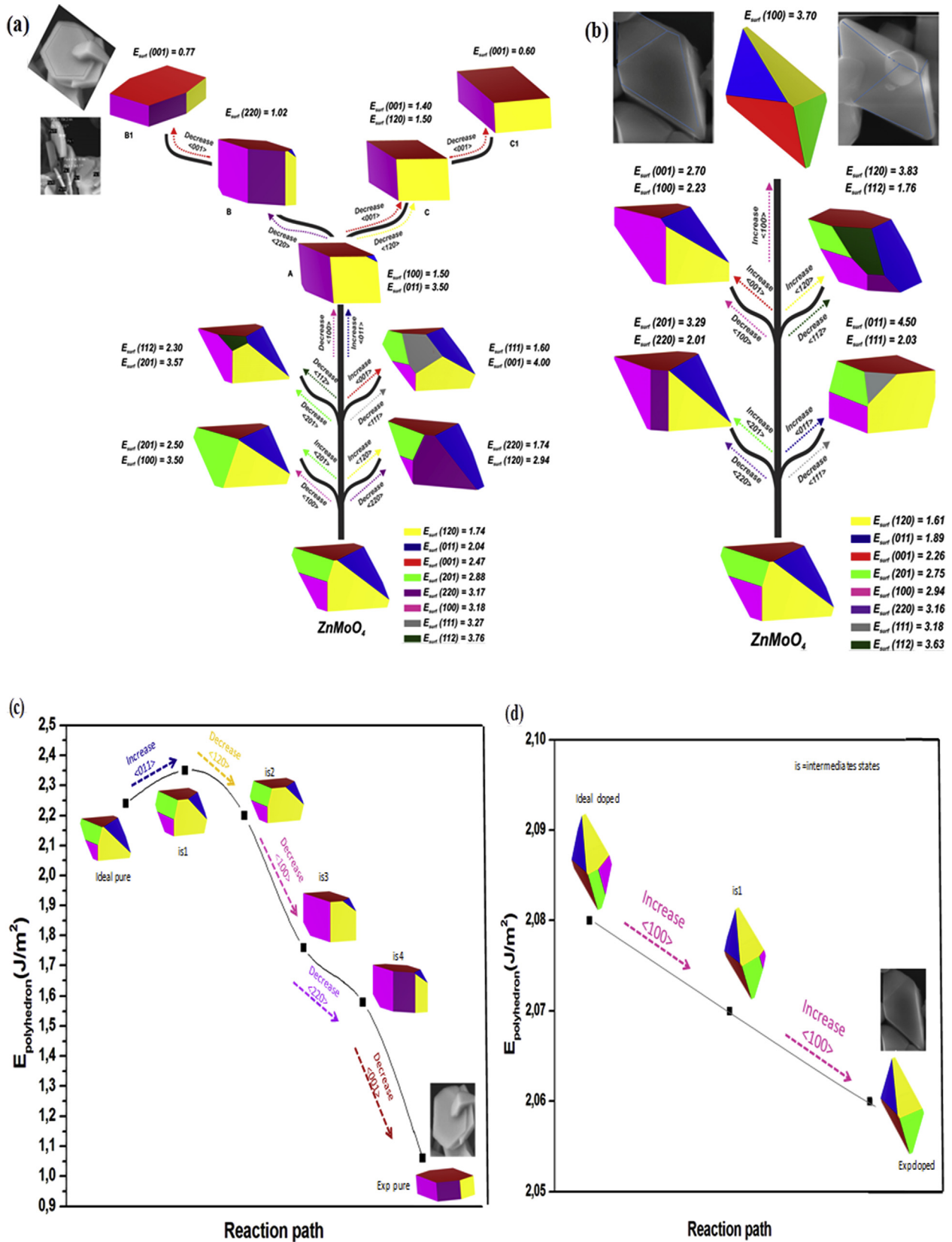


Fig. 12. (continued).





**Fig. 13.** Morphology map of (a) ZnMoO<sub>4</sub> and (b) ZnMoO<sub>4</sub>:12.5% mol Eu<sup>3+</sup> crystals obtained from Wulff's construction. The values of  $E_{surf}$  for (120), (011), (001), (201), (100), (220), (111), and (112) surfaces are employed. Surface energy is in  $J m^{-2}$ .

the supplementary information. According to our results, the order of stability is as follows: (120) > (001) > (011) faces in the ideal model. Initially, it was calculated the ideal morphology of  $\text{ZnMoO}_4$  and  $\text{ZnMoO}_4:\text{Eu}^{3+}$  from the  $E_{\text{surf}}$ , and it is constituted by 33% (33%) of (120) surface, 23% (24%) of (001) surface, 22% (24%) of (011) surface, 16% (14%) of (201) surface, and 6% (7%) of (100) surface, being the values in parenthesis for  $\text{ZnMoO}_4:12.5\% \text{ mol Eu}^{3+}$ .

The available morphologies for both  $\text{ZnMoO}_4$  and  $\text{ZnMoO}_4:12.5\% \text{ mol Eu}^{3+}$  systems can be obtained modifying the relative values of the surface energies or each surface, as it is shown in Fig. 13(a and b). In this map, it is found the experimental morphology obtained for  $\text{ZnMoO}_4$  in the present work, by means of the following paths: from the ideal morphology by increasing and/or decreasing the  $E_{\text{surf}}$  value of (011), (100), (220) and (001) surfaces as shown in Fig. 13a. The morphology reported by Jia et al. and Wang et al. [86,87] can be reached following the path from A to C and to C1 paths, respectively. Jia et al. synthesized  $\text{ZnMoO}_4$  by hydrothermal method in conditions of different template agents and the as-prepared products presented varied morphologies for the same crystalline phase (monoclinic), showing in Fig. 13a the corresponding morphology. Wang et al. prepared  $\text{ZnMoO}_4$  via a hydrothermal route with the increase in the monomer concentrations and the influence of temperature on the shape of  $\text{ZnMoO}_4$  was also investigated, reporting a transition from monoclinic to triclinic phase.

The experimental morphology of  $\text{ZnMoO}_4:\text{Eu}^{3+}$  was reached by increasing the value of  $E_{\text{surf}}$  for (100) surface to  $3.70 \text{ J/m}^2$  as illustrated in Fig. 13b. It is known that a change of morphologies can occur because of the presence of surfactants, impurities, temperature, synthetic routes and other factors. Furthermore, in this work, it is proposed a theoretical strategy for obtaining a reaction path, assuming the creation and screening of alternative reaction routes (intermediate states), to lead to a desired morphology, as presented in Fig. 13(c and d). Therefore, the values of  $E_{\text{surf}}$  from the calculated ideal morphology were used (Fig. 13(c and d)) to predict the intermediate states to lead to a desired morphology (experimental), and this strategy allows us to rationalize the different reaction paths to pass the corresponding energy barriers and to control the crystal morphologies.

#### 4. Conclusions

Searching for new classes of inorganic materials, which emerge as a promising option in high-performance applications in the field of photoluminescence, has received special attention. Particularly, oxides doped with rare earth ( $\text{RE}^{3+}$ ) elements present high luminous efficiency, long decay time and emissions in their visible region.

In the present work,  $\text{ZnMoO}_4$  and  $\text{ZnMoO}_4:\text{RE}^{3+} = \text{Tb}^{3+} - \text{Tm}^{3+} - x \text{Eu}^{3+}$  ( $x = 1, 1.5, 2, 2.5$  and  $3 \text{ mol \%}$ ) crystals were successfully synthesized using the sonochemical method. XRD observation revealed good crystallinity of the samples prepared without any impurities. All samples showed light emission in the orange–red region. Experimental results and first-principles calculations show a reduction in Egap values provoked by the structural defects and changes of the electronic structure promoted by the introduction of  $\text{RE}^{3+}$  in the  $\text{ZnMoO}_4$  lattice. We have for the first time demonstrated that the sample  $\text{ZnMoO}_4: 1\% \text{ Tb}^{3+}, 1\% \text{ Tm}^{3+}, 2\% \text{ Eu}^{3+}$ , present a larger photoluminescence intensity. At higher concentrations of  $\text{RE}^{3+}$ , the quenching effect was observed. The structural and band gap relationship points out the possibility of band gap engineering in these materials through composition modulation.

FEG-SEM images revealed that both  $\text{ZnMoO}_4$  and  $\text{ZnMoO}_4:12.5\% \text{ Eu}^{3+}$  samples exhibited similar morphologies. First-principle calculations, at density functional theory level, were performed to

obtain the values of surface energies and relative stability of the (120), (001), (011), (201), and (100) surfaces and Wulff construction is employed to rationalize the crystal morphologies found by FE-SEM images. A complete map of the morphologies available for  $\text{ZnMoO}_4$  and  $\text{ZnMoO}_4:12.5\% \text{ mol Eu}^{3+}$  is obtained and a possible explanation for the transformation processes is provided in which the experimental and theoretical morphologies can match. The present study provided fundamental knowledge on  $\text{ZnMoO}_4$ , and the method of controlling its color emission. Then, a new strategy for the rational structural design of  $\text{ZnMoO}_4:\text{RE}^{3+}$  crystals for optoelectronic applications is presented.

#### Acknowledgements

The authors gratefully acknowledge the financial support of the Brazilian governmental research funding agencies CAPES, CNPq, FAPESP and INCTMN. J.A. acknowledge Generalitat Valenciana for *PrometeoII/2014/022*, *ACOMP/2014/270*, and *ACOMP/2015/1202*, and Ministerio de Economía y Competitividad (Spain) project *CTQ2015-65207-P* for financially supporting this research. M.C. acknowledges Generalitat Valenciana for the Santiago Grisolia Program 2015/033. We also acknowledge the Servei Informàtica, Universitat Jaume I for a generous allotment of computer time.

#### Appendix A. Supplementary data

Supplementary data related to this article can be found at <https://doi.org/10.1016/j.jallcom.2018.03.394>.

#### References

- [1] Y. Yang, X. Li, W. Feng, W. Yang, W. Li, C. Tao, Effect of surfactants on morphology and luminescent properties of  $\text{CaMoO}_4:\text{Eu}^{3+}$  red phosphors, *J. Alloys. Compd.* 509 (2011) 845.
- [2] Y. Jin, J. Zhang, Z. Hao, X. Zhang, Synthesis and luminescence properties of clew-like  $\text{CaMoO}_4:\text{Sm}^{3+}, \text{Eu}^{3+}$ , *J. Alloys. Compd.* 509 (2011) L348.
- [3] J.H. Chung, S.Y. Lee, K.B. Shim, S.-Y. Kweon, S.-C. Ur, J.H. Ryu, Blue upconversion luminescence of  $\text{CaMoO}_4:\text{Li}^+/\text{Yb}^{3+}/\text{Tm}^{3+}$  phosphors prepared by complex citrate method, *Appl. Phys. A* 108 (2012) 369.
- [4] J. Fei, Q. Sun, J. Li, Y. Cui, J. Huang, W. Hui, H. Hu, Synthesis and electrochemical performance of  $\alpha\text{-ZnMoO}_4$  nanoparticles as anode material for lithium ion batteries, *Mater. Lett.* 198 (2017) 4–7.
- [5] W.N. Wang, Y. Kaihatsu, F. Iskandar, K. Okuuama, Highly luminous hollow chloroapatite phosphors formed by a template-free aerosol route for solid-state lighting, *Chem. Mater.* 21 (2009) 4685.
- [6] E.F. Schubertand, J.K. Kim, Solid-state light sources getting smart, *Science* 308 (2005) 1274.
- [7] A.A. Talin, K.A. Dean, J.E. Jaskie, Field emission displays: a critical review, *Solid State Electron.* 45 (2001) 963.
- [8] B.V. Ratnam, M. Jayasimhadri, Kiwan Jang, H.S. Lee, Y. Soung-Soo, J.H. Jeong, White light emission from  $\text{NaCaPO}_4:\text{Dy}^{3+}$  phosphor for ultraviolet-based white light-emitting diodes, *J. Am. Ceram. Soc.* 93 (2010) 3857.
- [9] O.S. Wolfbeis, Lanthanide Luminescence, Springer, New York, 2011.
- [10] B.G. Wybourne, Optical Spectroscopy of Lanthanides, CRC Press, Taylor and Francis, Boca Raton, USA, 2007.
- [11] B.P. Maheshwary, J. Singh, R.A. Singh, Luminescence properties of  $\text{Eu}^{3+}$  activated  $\text{SrWO}_4$  nanophosphors-concentration and annealing, *RSC Adv.* 4 (2015) 32605.
- [12] X. Li, Y. Zhang, D. Geng, J. Lian, G. Zhang, Z. Hou, J. Lin,  $\text{CaGdAlO}_4:\text{Tb}^{3+}/\text{Eu}^{3+}$  as promising phosphors for full-color field emission displays, *J. Mater. Chem. C* 2 (2014) 9924.
- [13] R.S. Ningthoujam, in: S.B. Rai, Y. Dwivedi (Eds.), Enhancement of luminescence by rare earth ions doping in semiconductor host, 6, Nova Science Publishers Inc., 2012, pp. 145–182.
- [14] N. Jaina, B.P. Singhb, R.K. Singha, J. Singha, R.A. Singh, Enhanced photoluminescence behaviour of  $\text{Eu}^{3+}$  activated  $\text{ZnMoO}_4$  nanophosphors via  $\text{Tb}^{3+}$  co-doping for light emitting diode, *J. Lumin.* 188 (2017) 504–513.
- [15] A. Pandey, V.K. Rai, V. Kumar, V. Kumar, H.C. Swart, Upconversion based temperature sensing ability of  $\text{Er}^{3+}-\text{Yb}^{3+}$  codoped  $\text{SrWO}_4$ : an optical heating phosphor, *Sens. Actuators, B* 209 (2015) 352.
- [16] J.A. Dorman, J.H. Choi, G. Kuzmanich, J.P. Chang, High-quality white light using core–shell  $\text{RE}^{3+}:\text{LaPO}_4$  ( $\text{RE} = \text{Eu}, \text{Tb}, \text{Dy}, \text{Ce}$ ) phosphors, *J. Phys. Chem. C* 116 (2012) 12854.
- [17] B.P. Singh, A.K. Parchur, R.S. Ningthoujam, A.A. Ansari, P. Singh, S.B. Rai, Enhanced photoluminescence in  $\text{CaMoO}_4:\text{Eu}^{3+}$  by  $\text{Gd}^{3+}$  co-doping, *Dalton*

- Trans. 43 (2014) 4779.
- [18] Y. Jin, J. Zhang, S. Lu, H. Zhao, X. Zhang, X.J. Wang, Fabrication of  $\text{Eu}^{3+}$  and  $\text{Sm}^{3+}$  codoped micro/nanosized  $\text{MMoO}_4$  ( $M = \text{Ca}, \text{Ba}, \text{and Sr}$ ) via facile hydrothermal method and their photoluminescence properties through energy transfer, *J. Phys. Chem. C* (2008), 1125860.
- [19] M. Yang, Y. Liang, Q. Gui, B. Zhao, D. Jin, M. Lin, L. Yan, H. You, L. Dai, Y. Liu, Multifunctional luminescent nanomaterials from  $\text{NaLa}(\text{MoO}_4)_2:\text{Eu}^{3+}/\text{Tb}^{3+}$  with tunable decay lifetimes, emission colors, and enhanced cell viability, *Sci. Rep.* 5 (2015) 11844.
- [20] F. Wang, X. Liu, Upconversion multicolor fine-tuning: visible to near-infrared emission from lanthanide-doped  $\text{NaYF}_4$  nanoparticles, *J. Am. Chem. Soc.* 130 (2008) 5642.
- [21] N. Niu, P. Yang, F. He, X. Zhang, S. Gai, C. Li, Lin, Tunable multicolor and bright white emission of one-dimensional  $\text{NaLuF}_4:\text{Yb}^{3+}, \text{Ln}^{3+}$  ( $\text{Ln} = \text{Er}, \text{Tm}, \text{Ho}, \text{Er}/\text{Tm}, \text{Tm}/\text{Ho}$ ) microstructures, *J. Mater. Chem.* vol. 22 (2012) 10889.
- [22] V. Ya. Degoda, Ya. P. Kogut, I.M. Moroz, F.A. Danevich, Long time phosphorescence in  $\text{ZnMoO}_4$  crystals, *J. Lumin.* 181 (2017) 269–276.
- [23] V. Ya. Degoda, Ya. P. Kogut, I.M. Moroz, F.A. Danevich, Thermally stimulated luminescence in  $\text{ZnMoO}_4$  crystals, *J. Lumin.* 183 (2017) 424–432.
- [24] V. Ya. Degoda, Ya. P. Koguta, I.M. Moroz, F.A. Danevich, S.G. Nasonov, E.P. Makarov, V.N. Shlegel, Temperature dependence of luminescence intensity in  $\text{ZnMoO}_4$  crystals, *Mater. Res. Bull.* 89 (2017) 139–149.
- [25] D. Spassky, V. Nagirnyi, S. Vielhauer, H. Mägi, S.G. Nasonov, V.N. Shlegel, A. Belsky, Emission centers in  $\text{ZnMoO}_4$ : influence of growth conditions and decay characteristics, *Opt. Mater.* 59 (2016) 66–69.
- [26] M.A. Patel, B.A. Bhanvase, S.H. Sonawane, Production of cerium zinc molybdate nano pigment by innovative ultrasound assisted approach, *Ultrason. Sonochem.* 20 (2013) 906–913.
- [27] Z. Shahri, M. Bazarganipour, M. Salavati-Niasari, Controllable synthesis of novel zinc molybdate rod-like nanostructures via simple surfactant-free precipitation route, *Superlattice. Microsc.* 63 (2013) 258–266.
- [28] C.C. Mardare, D. Tanasic, A. Rathner, N. Muller, A.W. Hassel, Growth inhibition of *Escherichia coli* by zinc molybdate with different crystalline structure, *Phys. Status Solidi A* 213 (2016) 1471–1478.
- [29] L. Wan, J. Shen, Y. Zhang, X. Li, Novel  $\text{ZnMoO}_4/\text{reduced graphene oxide}$  hybrid as a high-performance anode material for lithium ion batteries, *J. Alloys. Compd.* 708 (2017) 713–721.
- [30] S. Dutta, S. Som, S.K. Sharma, Luminescence and photometric characterization of  $\text{K}^+$  compensated  $\text{CaMoO}_4:\text{Dy}^{3+}$  nanophosphors, *Dalton Trans.* 42 (2013) 9654.
- [31] W. Reichelt, T. Weber, T. Söhnel, S. Däbritz, Mischkristallbildung im System  $\text{CuMoO}_4/\text{ZnMoO}_4$ , *Z. Anorg. Allg. Chem.* 626 (2000) 2020–2027.
- [32] T. Söhnel, W. Reichelt, H. Oppermann, H.J. Mattauch, A. Simon, Zum System  $\text{Zn}/\text{Mo}/\text{O}$ . I. Phasenbestand und Eigenschaften der ternären Zinkmolybdate; Struktur von  $\text{Zn}_3\text{Mo}_2\text{O}_9$ , *Z. Anorg. Allg. Chem.* 622 (1996) 1274.
- [33] K. Pavani, A. Ramanan, Influence of 2-aminopyridine on the formation of molybdates under hydrothermal conditions, *Eur. J. Inorg. Chem.* 2005 (2005) 3080–3087.
- [34] V.B. Mikhailik, H. Kraus, D. Wahl, H. Ehrenberg, M.S. Mykhayl, Optical and luminescence studies of  $\text{ZnMoO}_4$  using vacuum ultraviolet synchrotron radiation, *Nucl. Instrum. Meth. Phys. Res. A* 562 (2006) 513.
- [35] J.C. Sczancoski, L.S. Cavalcante, N.L. Marana, R.O. da Silva, R.L. Tranquillin, M.R. Joya, P.S. Pizani, J.A. Varela, J.R. Sambrano, M. Siu Li, E. Longo, J. Andrés, Electronic structure and optical properties of  $\text{BaMoO}_4$  powders, *Curr. Appl. Phys.* 10 (2010) 614.
- [36] L.S. Cavalcante, J.C. Sczancoski, M. Siu Li, E. Longo, J.A. Varela,  $\beta$ -ZMO microcrystals synthesized by the surfactant-assisted hydrothermal method: growth process and photoluminescence properties, *Colloid. Surface. Physicochem. Eng. Aspect.* 396 (2012) 346.
- [37] X. JU, X. LI, W. LI, W. YANG, C. TAO, Luminescence properties of  $\text{ZMO}:\text{Tb}^{3+}$  green phosphor prepared via co-precipitation, *Mater. Lett.* 65 (2011) 2642.
- [38] P. Li, L. Pang, Z. Wang, Z. Yang, Q. Guo, X. Li, Luminescent characteristics of  $\text{LiBaBO}_3:\text{Tb}^{3+}$  green phosphor for white LED, *J. Alloys. Compd.* 478 (2009) 813.
- [39] J. Llanos, R. Castillo, W. Alvarez, Preparation, characterization and luminescence of a new green-emitting phosphor:  $\text{Gd}_2\text{TeO}_6$  doped with  $\text{Tb}^{3+}$ , *Mater. Lett.* 62 (2008) 3597.
- [40] X. Li, Z. Yang, L. Guan, Q. Guo, A new yellowish green luminescent material  $\text{SrMoO}_4:\text{Tb}^{3+}$ , *Mater. Lett.* 63 (2009) 1096.
- [41] T. Chengaiah, C.K.A. Jayasankar, K. Pavani, T. Sasikala, L.R. Moorthy, Preparation and luminescence characterization of  $\text{Zn}(1-x)\text{MoO}_4:\text{xDy}^{3+}$  phosphor for white light-emitting diodes, *Optic Commun.* 312 (2014) 233.
- [42] W. Ran, L. Wang, W. Zhang, F. Li, H. Jiang, W. Li, L. Su, R. Houzong, X. Pana, J. Shi, A super energy transfer process based S-shaped cluster in ZMO phosphors: theoretical and experimental investigation, *J. Mater. Chem. C* 3 (2015) 8344.
- [43] C.T. Lee, W.T. Yang, R.G. Parr, Development of the Colle-Salvetti correlation-energy formula into a functional of the electron density, *Phys. Rev. B Condens. Matter* 37 (1988) 785–789.
- [44] A.D. Becke, Perspective on “Density functional thermochemistry. III. The role of exact exchange”, *J. Chem. Phys.* 98 (1993) 5648–5652.
- [45] R. Dovesi, R. Orlando, A. Erba, C.M. Zicovich-Wilson, B. Civalieri, S. Casassa, et al., CRYSTAL14: a program for the ab initio investigation of crystalline solids, *Int. J. Quant. Chem.* 114 (2014) 1287–1317.
- [46] Access to the site: [http://www.crystal.unito.it/Basis\\_Sets/europium.html](http://www.crystal.unito.it/Basis_Sets/europium.html).
- [47] F. Corà, A. Patel, N.M. Harrison, C. Roetti, C.R.A. Catlow, An ab-initio Hartree-Fock study of  $\alpha\text{-MoO}_3$ , *J. Mater. Chem.* 7 (1997) 959–967.
- [48] C. Gatti, V.R. Saunders, C. Roetti, Crystal field effects on the topological properties of the electron density in molecular crystals: the case of urea, *J. Chem. Phys.* 101 (1994) 10686–10696.
- [49] T. Homann, U. Hotje, M. Binnewies, A. Borger, K.D. Becker, T. Bredow, Composition-dependent band gap in  $\text{ZnSxSe1-x}$ : a combined experimental and theoretical study, *Solid State Sci.* 8 (2006) 44–49.
- [50] H.J. Monkhorst, J.D. Pack, Special points for Brillouin-zone integrations, *Phys. Rev. B* 13 (1976) 5188.
- [51] G. Wulff, Xv, Zur frage der geschwindigkeit des wachstums und der auflösung der krystallflächen, *Z. für Kristallogr. - Cryst. Mater.* 34 (1901) 449–530.
- [52] M. Bomio, R. Tranquilin, F.V. Motta, C.A. Paskocimas, R.M. Nascimento, L. Gracia, J. Andrés, E. Longo, Towards understanding the photocatalytic activity of  $\text{PbMoO}_4$  powders with predominant (111), (100), (011), and (110) facets. A combined experimental and theoretical study, *J. Phys. Chem. C* 117 (2013) 21382–21395.
- [53] M.T. Fabbro, C. Saliby, L.R. Rios, F.A. La Porta, L. Gracia, M.S. Li, Identifying and rationalizing the morphological, structural, and optical properties of  $\beta\text{-Ag}_2\text{MoO}_4$  microcrystals, and the formation process of Ag nanoparticles on their surfaces: combining experimental data and first-principles calculations, *Sci. Technol. Adv. Mater.* 16 (2015) 65002–65011.
- [54] M.C. Oliveira, et al., On the morphology of  $\text{BaMoO}_4$  crystals: a theoretical and experimental approach, *Cryst. Res. Technol.* 51 (2016) 634–644.
- [55] H.P. Klug, L.E. Alexander, X-Ray Diffraction Procedures, 1959 (New York).
- [56] Y. Gao, Y. Sun, H. Zou, Y. Sheng, X. Zhou, B. Zhang, B. Zhou, Effect of  $\text{Eu}^{3+}$  doping on the structural and photoluminescence properties of cubic  $\text{CaCO}_3$ , *Mater. Sci. Eng. B* 203 (2016) 52.
- [57] Y.S. Vidya, K.S. Anantharaju, H. Nagabhushana, S.C. Sharma, H.P. Prashantha, C. Shivakumara, Combustion synthesized tetragonal  $\text{ZrO}_2:\text{Eu}^{3+}$  nanophosphors: structural and photoluminescence studies, *Spectrochim. Acta Mol. Biomol. Spectrosc.* 135 (2015) 241–251.
- [58] A. Kokalj, Computer graphics and graphical user interfaces as tools in simulations of matter at the atomic scale, *Comput. Mater. Sci.* 28 (2003) 155.
- [59] D.L. Wood, J. Tauc, Weak absorption tails in amorphous semiconductors, *Phys. Rev. B* 5 (1972) 3144.
- [60] R. Lacombe-Perales, J. Ruiz-Fuertes, D. Errandonea, D. Martinez-Garcia, A. Segura, Optical absorption of divalent metal tungstates: correlation between the band-gap energy and the cation ionic radius, *Eur. Phys. Lett.* 83 (2008) 37002.
- [61] I.L. Validzic, T.D. Savic, R.M. Krstanovic, D.J. Jovanovic, M.M. Novakovic, M.C. Popovic, M.I. Comor, Synthesis, strong room-temperature PL and photocatalytic activity of  $\text{ZnO}/\text{ZnWO}_4$  rod-like nanoparticles, *Mater. Sci. Eng. B* 177 (2012) 645.
- [62] J. Ruiz-Fuertes, S. Lopez-Moreno, J. Lopez-Solano, D. Errandonea, A. Segura, R. Lacombe-Perales, A. Munoz, S. Radescu, P. Rodriguez-Hernandez, M. Gospodinov, L.L. Nagornaya, C.Y. Tu, Pressure effects on the electronic and optical properties of  $\text{AWO}_4$  wolframites ( $A = \text{Cd}, \text{Mg}, \text{Mn}, \text{and Zn}$ ): the distinctive behavior of multiferroic  $\text{MnWO}_4$ , *Phys. Rev. B* 86 (2012), 125202.
- [63] J. Liu, H. Lian, C. Shi, Improved optical photoluminescence by charge compensation in the phosphor system  $\text{CaMoO}_4:\text{Eu}^{3+}$ , *Opt. Mater.* 29 (2007) 1591.
- [64] V.M. Longo, L.S. Cavalcante, R. Erlo, V.R. Mastelaro, A.T. de Figueiredo, J.R. Sambrano, S. de Lazaro, A.Z. Freitas, L. Gomes, N.D. Vieira Jr., J.A. Varela, E. Longo, Strong violet–blue light photoluminescence emission at room temperature in  $\text{SrZrO}_3$ : joint experimental and theoretical study, *Acta Mater.* 56 (2008) 2191.
- [65] X.Y. Wu, J. Du, H.B. Li, M.F. Zhang, B.J. Xi, H. Fan, Y.C. Zhu, Y.T. Qian, Aqueous mineralization process to synthesize uniform shuttle-like  $\text{BaMoO}_4$  microcrystals at room temperature, *J. Solid State Chem.* 180 (2007) 3288.
- [66] S.S. Ding, M. Lei, H. Xiao, G. Liu, Y.C. Zhang, K. Huang, C. Liang, Y.J. Wang, R. Zhang, D.Y. Fan, H.J. Yang, Y.G. Wang, Morphology evolution and photoluminescence of barium molybdate controlled by poly (sodium-4-styrenesulfonate), *J. Hernandez Appl. Phys. Lett.* 91 (2007), 051923. *Journal of Alloys and Compounds* 579 (2013) 549.
- [67] A.B. Campos, A.Z. Simões, E. Longo, J.A. Varela, V.M. Longo, A.T. de Figueiredo, F.S. De Vicente, A.C. Hernandez, Mechanisms behind blue, green, and red photoluminescence emissions in  $\text{CaWO}_4$  and  $\text{CaMoO}_4$  powders, *Appl. Phys. Lett.* 91 (2017), 051923.
- [68] A.P.A. Marques, F.V. Motta, E.R. Leite, P.S. Pizani, J.A. Varela, E. Longo, D.M.A. de Melo, Evolution of photoluminescence as a function of the structural order or disorder in  $\text{CaMoO}_4$  nanopowders, *J. Appl. Phys.* 104 (2008), 043505.
- [69] J.H. Ryu, J.W. Yoon, C.S. Lim, K.B. Shim, Microwave-assisted synthesis of barium molybdate by a citrate complex method and oriented aggregation, *Mater. Res. Bull.* 40 (2005) 1468.
- [70] A. Speghini, M. Bettinelli, Preparation, structural characterization and luminescence properties of  $\text{Eu}^{3+}$ -doped nanocrystalline  $\text{ZrO}_2$ , *J. Mater. Res.* 20 (2005) 2780–2789.
- [71] K. Binnemans, Interpretation of europium(III) spectra, *Coord. Chem. Rev.* 295 (2015) 1–45.
- [72] M. Inokuti, F. Hirayama, Influence of energy transfer by the exchange mechanism on donor luminescence, *J. Chem. Phys.* 4 (1965) 1978.
- [73] F. Wang, X.G. Liu, Recent advances in the chemistry of lanthanide-doped upconversion nanocrystals, *Chem. Soc. Rev.* 38 (2009) 976.
- [74] P. Jena, S.K. Gupta, V. Natarajan, M. Sahu, N. Satyanarayana, M. Venkateswarlu,

- Structural characterization and photoluminescence properties of sol–gel derived nanocrystalline BaMoO<sub>4</sub>:Dy<sup>3+</sup>, *J. Lumin.* 158 (2015) 203–210.
- [75] G. García-Rosales, et al., Energy transfer from Tb<sup>3+</sup> to Eu<sup>3+</sup> ions sorbed on SrTiO<sub>3</sub> surface, *J. Lumin.* 132 (2012) 1299–1306.
- [76] L.X. Lovisa, J. Andres, L. Gracia, M.S. Li, C.A. Paskocimas, M.R.D. Bomio, V.D. Araujo, E. Longo, F.V. Motta, Photoluminescent properties of ZrO<sub>2</sub>: Tm<sup>3+</sup>, Tb<sup>3+</sup>, Eu<sup>3+</sup> powders: A combined experimental and theoretical study, *J. Alloys. Compd.* 695 (2017) 3094–3103.
- [77] G. Blasse, Energy transfer in oxidic phosphors, *Philips Res. Rep.* 24 (1969) 131.
- [78] F. Kang, Y. Zhang, M. Peng, Controlling the energy transfer via multi luminescent centers to achieve white light/tunable emissions in a single-phased X2-Type Y<sub>2</sub>SiO<sub>5</sub>: Eu<sup>3+</sup>, Bi<sup>3+</sup> phosphor for ultraviolet converted LEDs, *Inorg. Chem.* 54 (2015) 1462.
- [79] E.F. Schubert, *Light Emitting Diodes*, Cambridge University Press, 2003.
- [80] R. Robertson, Computation of correlated color temperature and distribution temperature, *J. Opt. Soc. Am.* 58 (1968) 1528.
- [81] C. S. McCamy, Correlated Color Temperature as an Explicit Function of Chromaticity Coordinates, Wappingers Falls, New York 12590-1804.
- [82] P. Boutinaud, L. Sarakha, E. Cavalli, M. Bettinelli, P. Dorenbos, R. Mahiou, About red afterglow in Pr<sup>3+</sup> doped titanate perovskites, *J. Phys. D Appl. Phys.* 42 (2009) 045106–045112.
- [83] F.A. La Porta, A.E. Nogueira, L. Gracia, W.S. Pereira, G. Botelho, T.A. Mulinari, J. Andrés, E. Longo, An experimental and theoretical investigation on the optical and photocatalytic properties of ZnS nanoparticles, *J. Phys. Chem. Solid.* 103 (2017) 179–189.
- [84] C.H. Huo, B.S. Wu, P. Gao, Y. Yang, Y.W. Li, H. Jiao, The mechanism of potassium promoter: enhancing the stability of active surfaces, *Angew. Chem.* 123 (2011) 7541–7544.
- [85] C. Burda, X.B. Chen, R. Narayanan, M.A. El-Sayed, Chemistry and properties of nanocrystals of different shapes, *Chem. Rev.* 105 (2005) 1025–1102.
- [86] R.P. Jia, C. Zhang, J.Y. Xu, Morphology-controllable synthesis and characterization of ZnMoO<sub>4</sub> nanoparticles, *Adv. Mater. Res.* 624 (2012) 51–54.
- [87] Dongming Wang, Maozhan Huang, Yan Zhuang, Hai-lang Jia, Jianhua Sun, Mingyun Guan, Phase- and morphology-controlled synthesis of zinc molybdate for excellent photocatalytic property, *Eur. J. Inorg. Chem.* 16 (2017) 4939–4946.